Notched Ti-6Al-4V titanium bars under multiaxial fatigue: Synthesis of crack initiation life based on the averaged strain energy density

Giovanni Meneghetti[a] Alberto Campagnolo[a] Filippo Berto[b] Keisuke Tanaka[c]

Abstract

The fatigue life of notched components subjected to multiaxial loading conditions may be influenced by extrinsic mechanisms operating during crack propagation phase, such as sliding contact, friction and meshing between crack surfaces. These extrinsic mechanisms may disrupt the applicability of local approaches, such as that based on the strain energy density (SED) averaged over a structural volume having size R_0 and surrounding the crack initiation point. In the present contribution, the multiaxial fatigue behaviour of circumferentially notched specimens made of titanium grade 5 alloy, Ti-6Al-4V, has been analysed. Pure bending, pure torsion and in-phase as well as out-of-phase combined bending-torsion fatigue tests have been carried out on notched specimens characterized by two different root radii, namely 0.1 and 4 mm. Fatigue crack initiation and subsequent propagation have been monitored by adopting the direct current potential drop (DCPD) technique. In principle, crack initiation life has been defined when the initiated fatigue crack fractures the structural volume, which corresponds to a given potential drop increase calibrated by means of electrical finite element (FE) analyses. The structural volume size R_0has been determined by fatigue testing plain and sharp V-notched specimens under pure axial or pure torsion loadings. Finally, the averaged SED approach has been adopted to correlate the experimental fatigue results expressed in terms of crack initiation life, in order to reduce the effect of extrinsic mechanisms.

- **Previous** article in issue
- **Next** article in issue

Keywords

Titanium alloy
Fatigue notch effect
Potential drop method
Crack initiation
Averaged SED

1. Introduction

Several local approaches have been proposed in the literature to deal with notches of different severity undergoing multiaxial fatigue loading. As a general remark, fatigue damageis supposed to be governed by stress, strain or energy quantities, which are typically evaluated at the point of maximum stress when dealing with plain or bluntly notched components, while they are averaged close to the notch tip dealing with sharply notched components, where severe stress gradients exist. The reader is referred to [1], [2], [3] for a comprehensive review of the main local approaches.

By nature, local approaches estimate the fatigue life to initiate and propagate a crack under uniform, self-similar conditions. If extrinsic mechanisms start to operate during crack propagation, local fatigue models likely fail to estimate components' life. The extrinsic mechanisms inducing shielding effects during fatigue crack propagation have been classified by Ritchie [4], [5] in the following categories: geometrical shielding (i.e. crack deflection and crack branching), contact shielding (i.e. plasticity, corrosion, roughness and friction) and zone shielding (i.e. micro-cracks and mismatch of different phases).

As an example of these extrinsic mechanisms, an unexpected effect called "notch-strengthening" has recently been observed when bars weakened by circumferential notches were fatigue tested under pure torsion or combined axial-torsion multiaxial loadings [6], [7], [8], [9], [10], [11]: at a given applied net-section stress amplitude, notched specimensexhibited longer fatigue lives than plain ones. The notch-strengthening effect was observed in cylindrical specimens made of austenitic stainless steels [6], [7], [8], NiCrMo steel [9] and pure titanium [10]; on the other hand it was not observed in carbon steels [8], [12], [13]. Several researchers [11], [14], [15], [16], [17], [18] explained this phenomenon on the basis of the different cracking behaviour of the materials, which led to different morphologies of the fracture surfaces. As an example, Tanaka [11] observed factory-roof type fracture surfaces when testing bars made of an austenitic stainless steel, weakened by a circumferential notch and subjected to torsion fatigue loading. Consequently, the sliding contact and the meshing between crack surfaces, caused a retardation of the crack propagation phase. Conversely, in the case of notched bars made of carbon steel subjected to torsion fatigue loading, crack branching producing factory-roofs was almost negligible, which translated in reduced meshing between fracture surfaces and therefore absence of retarded crack propagation.

Extrinsic phenomena can be described by means of approaches mainly based on the definition of shielding stress intensity factors (SIFs), which reduce the nominal crack driving force to an effective value. The shielding SIFs can be defined by means of mathematical models of the crack tip stress fields, such as the CJP model [19], or they can be estimated from geometrical and physical models of the mechanisms acting at crack surfaces [4], [20], from the experimental measurement of the crack propagation rate drop due to crack closure[18] or from a statistical approach based on the ratio between the characteristic microstructural distance and the plastic zone size [21]. Alternatively, extrinsic phenomena can be modelled also by using non-linear fracture mechanics simulations [22], [23]. However, as far as un-cracked geometries are considered in local fatigue models, it appears reasonable to estimate the sole crack initiation life, in order to reduce the influence of the extrinsic mechanisms, which often operate with increasing effectiveness as crack propagation proceeds.

In this context, “crack initiation” must be defined. In the present paper the local fatigue criterion first proposed by Lazzarin and Zambardi [24] has been employed. It is based on the strain energy density (SED) averaged over a structural volume surrounding the notch tip and having radius R_0. Recently [25], it has been highlighted that the crack initiation life should be considered in the SED-based re-analyses in order to reduce the effects of extrinsic mechanisms which act during the propagation phase, i.e. sliding contact, friction and meshing between fracture surfaces. A reasonable definition of “crack initiation” in relation to the local SED-approach can be singled-out when the initiated crack depth *a* equals R_0, i.e. when the crack depth leads to the structural volume failure. Several experimental techniquesexist to monitor small propagating cracks [26], [27], such as replication, photo-microscopy, electrical potential drop and scanning electron microscopy, which are covered by ASTM E647 [28], and also additional techniques based on surface acoustic waves, laser interferometry, ultrasonic, and eddy current techniques. In the present paper, the direct current potential drop (DCPD) technique has been adopted and calibrated to correlate the observed potential drop to the crack size.

In this paper, the multiaxial fatigue behaviour of circumferentially notched bars made of titanium grade 5 alloy, i.e. Ti-6Al-4V, has been analysed in relation to crack initiation life. Pure bending, pure torsion and combined in-phase as well as out-of-phase bending-torsion fatigue loadings have been applied to bars weakened by sharp, $\rho = 0.1$ mm, or blunt, $\rho = 4$ mm, notches to investigate the effect of both notch geometry and loading conditions on the fatigue strength. After summarising the theoretical background of the SED approach to multiaxial fatigue, the new test results of multiaxial notch fatigue with DCPD monitoring are presented; after that, the structural volume size R_0, which is peculiar of the SED approach, is estimated by means of pure axial and pure torsion fatigue tests on plain and severely notched specimens. After having determined the structural volume size, the fatigue life to initiate a crack of the same dimension is determined by using the calibration curves of the potential drop method previously found by means of electrical finite element (FE) analyses; in this context, limitations of the DCPD technique are illustrated. Finally, the SED approach is adopted to correlate the experimental fatigue results expressed in terms of crack initiation life.

2. Averaged strain energy density (SED) approach

The linear elastic strain energy density (SED), $\Delta \overline{W}$ (see Fig. 1a), averaged over a material-dependent control volume surrounding the crack initiation point (see Fig. 1b and c) has originally been proposed by Lazzarin and Zambardi [24] as a fatigue damage parameter for notched components.

$$(1)\Delta \overline{W} = \Delta W A$$

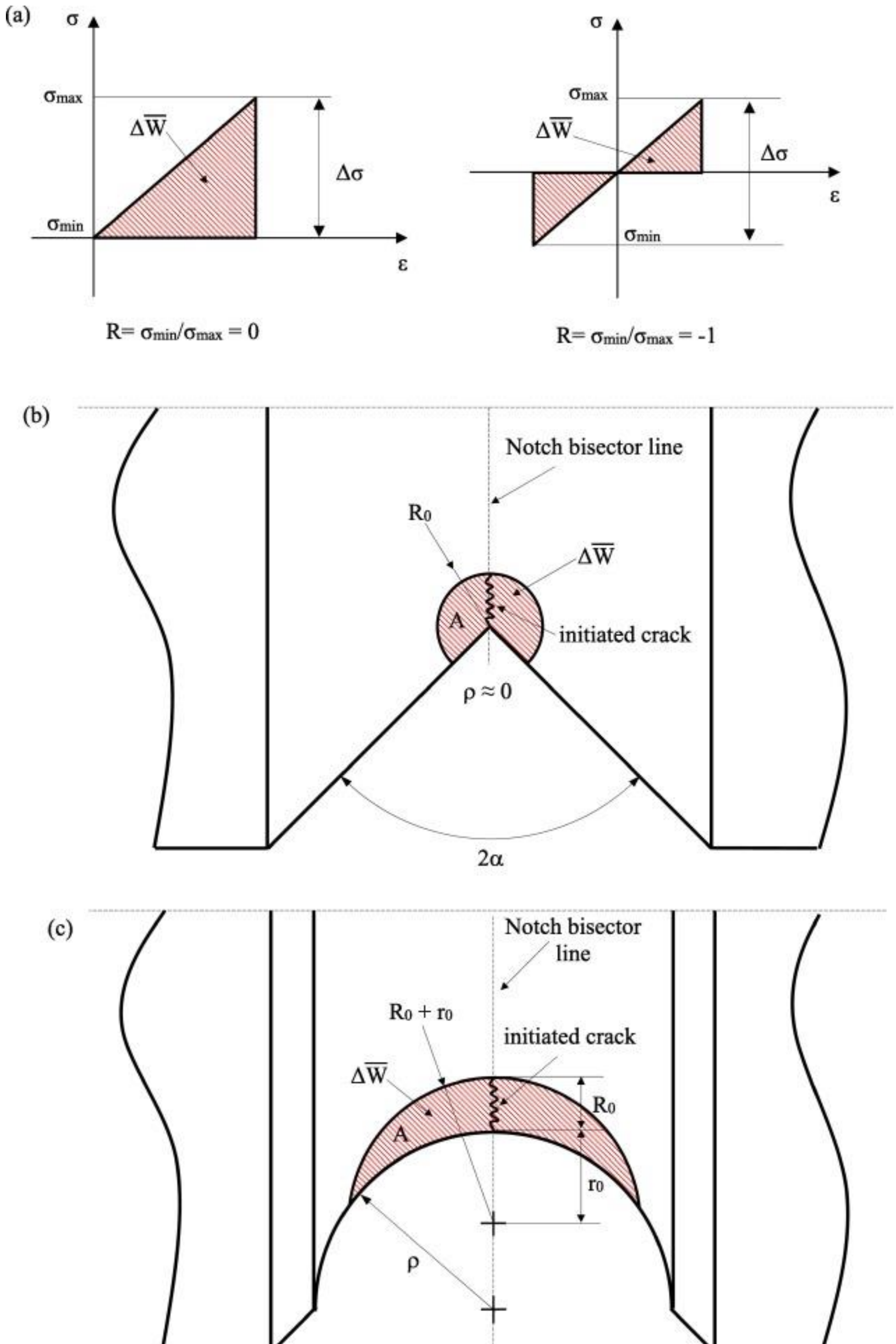
(a)
σ
σmax
σmin
ΔW̄
Δσ
ε
R= σmin/σmax = 0
σ
σmax
ΔW̄
Δσ
ε
σmin
R= σmin/σmax = -1
(b)
Notch bisector line
R0
ΔW̄
A
initiated crack
ρ ≈ 0
2α
(c)
Notch bisector line
R0 + r0
initiated crack
ΔW̄
A
R0
r0
ρ

1. Download high-res image (684KB)
2. Download full-size image

Fig. 1. (a) Strain energy density with nominal load ratios R = 0 and R = −1. Control volume to calculate the averaged SED for specimens with (b) a sharp [24] or (c) a blunt notch [37] and physical definition of crack initiation when *a* = R_0.

In the case of plain specimens, Eq. (1) can be applied under pure axial and pure torsionloadings as a function of the nominal net-section normal and shear stress range, respectively, according to the following expressions:

(2)ΔW¯=cWΔσ22Eplainspecimensunderaxialloading

(3)ΔW¯=cW(1+ν)Δτ2Eplainspecimensundertorsionloading

where the coefficient c_w accounts for the nominal load ratio R and it weights the stress range (see examples in Fig. 1a). In particular, c_w is defined by Eq. (4)[29] and equals 0.5 for R = −1.

(4)cw(R)=1+R2(1-R)2if-1⩽R⩽01-R2(1-R)2if0⩽R<1

The approach based on the averaged SED has its foundations on the fundamental idea proposed by Neuber [30], [31], [32], Peterson [33], Tanaka [34], Sheppard [35] and Taylor [36] of stress averaging over a material dependent microstructural length or volume. In the original contribution by Lazzarin and Zambardi [24], the SED approach has been theoretically formalized and applied to estimate both static and fatigue strength of sharp V-notched (ρ ≈ 0) components. Later on, the approach has been extended by Lazzarin and Berto [37] also to blunt U and V-notches with root radius greater than zero. The averaged SED approach proved to efficiently account for the notch-effect in structural componentsundergoing static [24], [38] or fatigue [24], [25], [39] loadings.

Dealing with the geometrical definition of the structural volume, the volume shape depends on the notch opening angle and on the notch tip radius:

- in the case of sharp V-notches, e.g. the specimens with notch tip radius ρ = 0.1 mm in next Fig. 3a and b, the structural volume is thought to be a circular sector of radius R_0, named “control radius” [24], with its center at the notch tip, as shown in Fig. 1b (A=(π-α)R02);

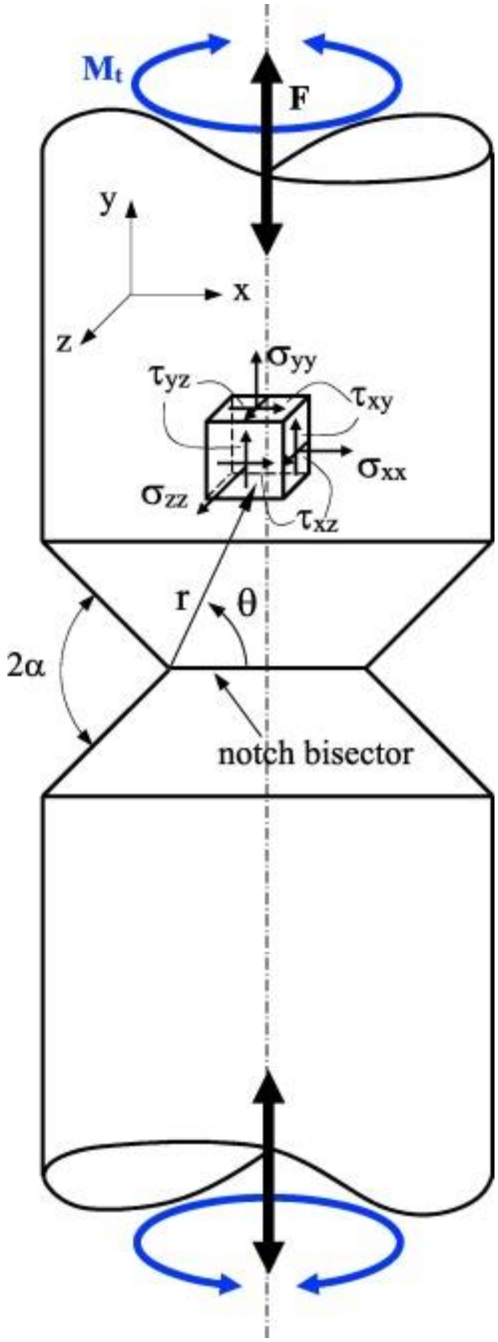

Fig. 2. Sharp V-notched bar subjected to axial (F) and torsion (M_t) loading. Cartesian stress components and polar coordinates (r, θ) with origin at the notch tip.

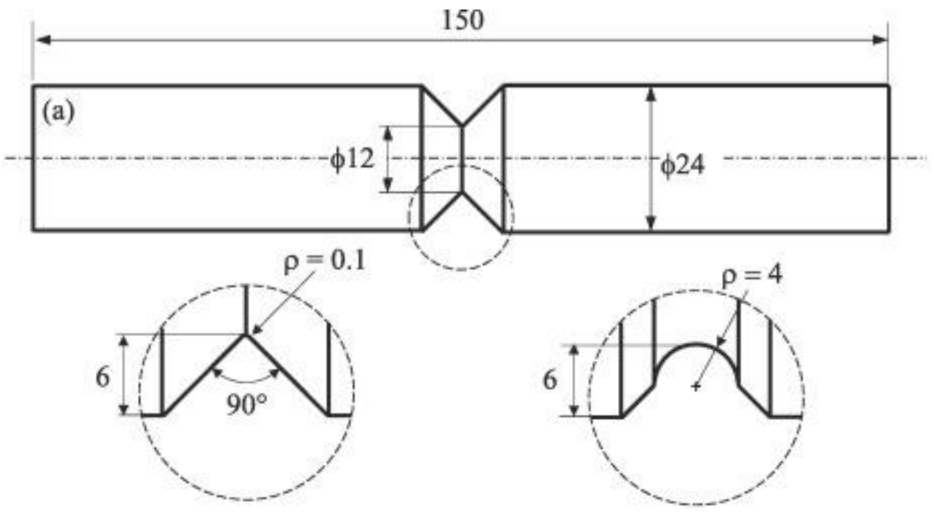

SN_ρ0.1_d_{net}12 BN_ρ4_d_{net}12

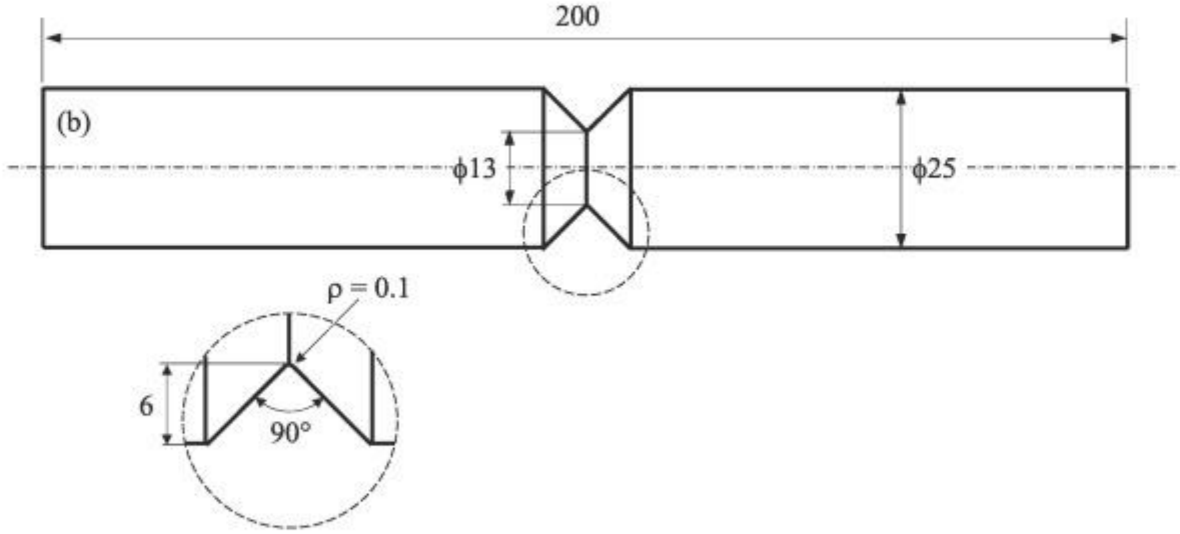

SN_ρ0.1_d_{net}13

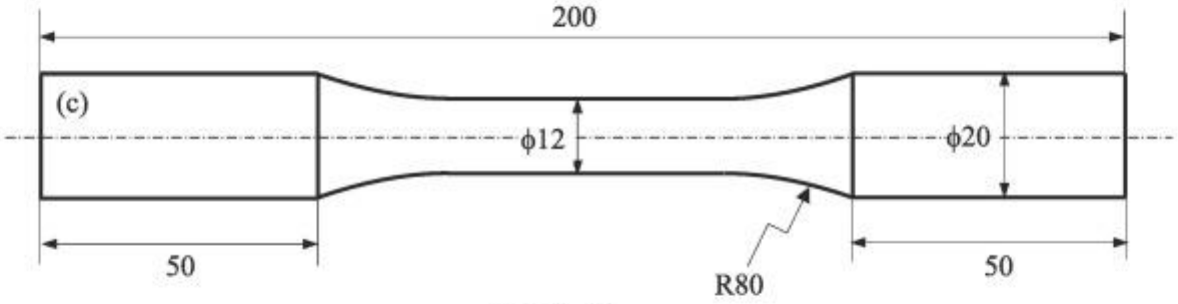

PL_d_{net}12

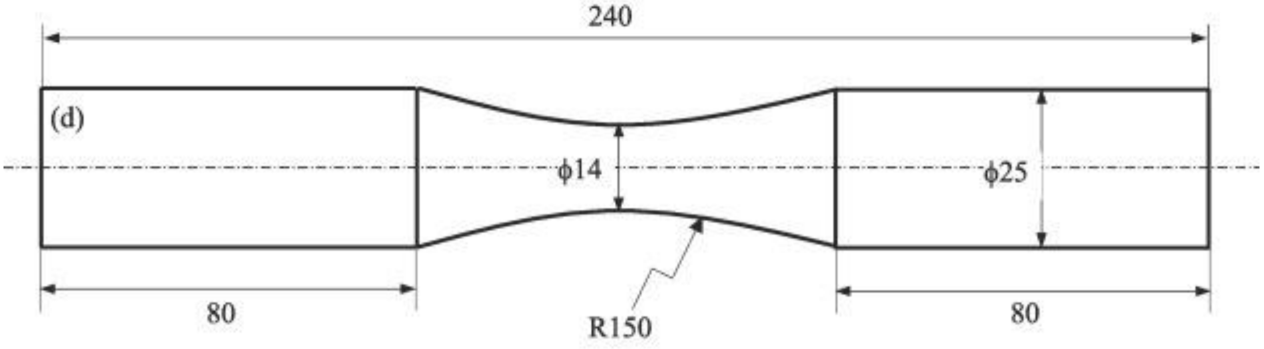

PL_d_{net}14

Fig. 3. Geometry of (a) and (b) circumferentially notched specimens and (c) and (d) plain specimens (dimensions are in mm).

- in the case of blunt notches, instead, e.g. the specimen with ρ = 4 mm in next Fig. 3a, Lazzarin and Berto [37] suggested that structural volume has the crescent shape detailed in Fig. 1c. In this case, R_0 is no longer a radius, but it represents the depth of the crescent shape measured along the notch bisector line. To properly model the structural volume, it is worth noting that the volume outer-radius is equal to $(R_0 + r_0)$, where r_0 is the distance between the notch tip and the volume center, which can be derived from Eq. (5), given the notch opening angle 2α and the notch tip radius ρ:

$$r_0 = \frac{q-1}{q}\rho \quad \text{where} \quad q = \frac{2\pi - 2\alpha}{\pi} \tag{5}$$

The circular shape of the structural volume for averaged SED calculation as proposed by Lazzarin and Zambardi [24] is an engineering choice and it is reminiscent of the shape suggested by Sheppard [35] for assessing the high-cycle fatigue strength of notched components. Lazzarin and Berto [37] assumed the centre of the circular sector in the origin of the polar coordinate system of Neuber's conformal mapping. Such a reference system is typically adopted to describe the local stress field ahead of the tip of sharp or blunt notches (see Lazzarin and Tovo [40] and Filippi et al. [41] for some examples of analytical derivations of the local stress field). In the general case of a blunt V-notch with a radius ρ and opening angle 2α, the centre of the structural volume is located behind the notch tip at a distance r_0, which is a function of both ρ and 2α. Fig. 1c illustrates the geometry for $2\alpha = 0$. Therefore, the circular volume of a blunt V-notch ($\rho > 0$, $r_0 > 0$) has radius $(R_0 + r_0)$ and, on the opposite side, it is delimited by the curvilinear edge of the notch, so that a "crescent shape" geometry is obtained. In Ref. [37], to which the reader needs to refer for more details, it has been shown that the "crescent shape" for blunt notches coincide with the strain energy density contour iso-lines calculated from some FE models for different notch opening angles.

Concerning the estimation of the structural volume size R_0, it is straightforward to equate the averaged SED at the fatigue limit of two opposite geometrical situations, i.e. the plain and the sharp notch geometries [9], [24]. Hence, R_0 results from the combination of two material properties: the fatigue limit of plain specimens and the threshold value of the Notch Stress Intensity Factor (NSIF) range for sharp V-notches.

Accordingly, R_0 can be evaluated under pure axial (mode I) and pure torsion (mode III) fatigue loadings by adopting Eqs. (6), (7), respectively, as derived in [9], [24] by assuming plane strain hypothesis:

(6)$R0,I=2e1\cdot\Delta K1,th\Delta\sigma 011-\lambda 1$

(7)$R0,III=e31+\nu\cdot\Delta K3,th\Delta\tau 011-\lambda 3$

where $\Delta K_{1,th}$ and $\Delta K_{3,th}$ are the threshold values of the NSIF ranges under mode I and mode III, respectively, while $\Delta\sigma_0$ and $\Delta\tau_0$ are the material fatigue limits, relevant to pure axial and pure torsion loadings, respectively; λ_1 and λ_3 are the stress singularity exponents [42], [43], which are functions of the notch opening angle 2α. Finally, e_1 and e_3 are known coefficients, which are dependent of the notch opening angle 2α and of the Poisson's ratio ν [18], [31]. The NSIF values under mode I and mode III loadings are defined according to Gross and Mendelson [44]:

(8a)$\Delta K1=2\pi\cdot\lim r\rightarrow 0[(\Delta\sigma yy)\theta=0\cdot r1-\lambda 1]$

(8b)$\Delta K3=2\pi\cdot\lim r\rightarrow 0[(\Delta\tau yz)\theta=0\cdot r1-\lambda 3]$

In previous expressions, the stress components σ_{yy} and τ_{yz} are referred to the notch bisector line, identified by the angular coordinate $\theta = 0$ in Fig. 2.

According to Eqs. (6), (7), R_0 could be different under axial and torsion loading, therefore the SED contributions due to the two different loading modes have to be averaged in volumes of different size [9]. The idea of a loading-mode-dependent value of R_0 has firstly been suggested by Berto et al. [9] when re-analysing multiaxial fatigue data obtained from notched samples made of 39NiCrMo3 steel. The same concept has later been adopted in the SED-based fatigue strength assessments of notched specimens made of AISI 416 [45], cast iron EN-GJS400 [46] and Ti-6Al-4V [47], undergoing combined axial-torsional loadings. The approach to define the size of the structural volume under mode I and III loadings described above, even though of a local nature, does not take into account the micro-mechanisms occurring at the microstructure level and the driving fatigue response. In this respect there are several studies in the literature, among them some are mentioned herein [48], [49], [50], [51], [52], [53], [54], [55], [56], [57].

Once the size of the structural volumes, $R_{0,I}$ and $R_{0,III}$, is properly defined, previous Eq. (1)could be applied directly to post-process results of linear elastic FE analyses to evaluate the averaged SED, $\Delta\bar{W}$, in notched specimens (Fig. 3a and b), according to the so-called "direct approach". Under a general multiaxial mode I + III fatigue loading situation, the superposition principle applied to Eq. (1) results in Eq. (9), according to which the summation of the strain energies $W_{FEM,i}$ evaluated for each i-th finite element included in the structural volume (or area in 2D problems, as shown in Fig. 1b and c) having size $R_{0,I}$ for mode I and $R_{0,III}$ for mode III contributions, has to be divided by the relevant total volume:

$$\Delta\overline{W}=\Delta\overline{W}_I+\Delta\overline{W}_{III}=c_W\left[\sum_{V(R_{0,I})}\frac{W_{FEM,i}}{V(R_{0,I})}\right]_{axial/bending}+\left[\sum_{V(R_{0,III})}\frac{W_{FEM,i}}{V(R_{0,III})}\right]_{torsion} \quad (9)$$

Lazzarin et al. [58] have recently demonstrated that very coarse FE meshes can be used inside the control volume.

Eq. (9) does not take into account a possible phase-shift between the different load contributions. Therefore its applicability to the present experimental results will be verified later on.

3. Experimental set-up and methods

The tested material is a grade 5 titanium alloy, i.e. Ti-6Al-4V, whose mechanical properties and chemical composition are reported in Table 1, Table 2, respectively. The specimens' geometries are reported in Fig. 3 and summarised in Table 3, together with the adopted load parameters. Geometry (a) has been adopted to generate the uniaxial/multiaxial datasets(B,T, B + T $\phi = 0°$, B + T $\phi = 90°$) according to Table 3. Geometries (b), (c) and (d) have been used to calibrate the structural volume size R_0 under pure axial ($R_{0,I}$, Eq. (6)) and pure torsion ($R_{0,III}$, Eq. (7)) loadings.

Table 1. Mechanical properties of the considered titanium grade 5 alloy, Ti-6Al-4V.

σ_y (MPa)	σ_u (MPa)	E (MPa)	ν(–)	A (%)	Z (%)
915	980	110,000	0.3	13	29

Table 2. Chemical composition of the considered titanium grade 5 alloy, Ti-6Al-4V.

Fe (%)	O (%)	C (%)	N (%)	Al (%)	V (%)	H (%)	Residuals (%)	Ti (%)
0.13	0.15	0.02	0.03	6.05	3.98	0.001	<0.40	Balance

Table 3. Summary of specimens' geometries (see Fig. 3) and fatigue test results.

Specimen code^	ρ (mm)	d_{net}(mm)	d_{gross}(mm)	δ_I#(mm)	δ_V°(mm)	Load type*	$K_{t,net}$	# data	# runout	$\Delta\sigma_A$± or $\Delta\tau_A$±(MPa)	k**
SN_ρ0.1_d_{net}^{12}	0.1	12	24	40	16	B	5.85	5	2	336	10
						T	3.19	4	0	573	16
						B + T $\phi = 0°$	–	4	0	361	8
						B + T $\phi = 90°$	–	4	0	350	7

Specimen code[^]	**ρ (mm)**	**d_{net}(mm)**	**d_{gross}(mm)**	**δ_I[#](mm)**	**δ_V[°](mm)**	**Load type**[*]	**$K_{t,net}$**	**# data**	**# runout**	**$\Delta\sigma_A$[+] or $\Delta\tau_A$[+](MPa)**	**k**[**]
BN_ρ4_d_{net}^{12}	4	12	24	40	16	B	1.39	5	3	1011	22
						T	1.21	4	1	769	16
						B + T $\phi = 0°$	–	4	1	682	18
						B + T $\phi = 90°$	–	4	0	692	17
SN_ρ0.1_d_{net}^{13}	0.1	13	25	40	14	A	7.76	8	2	226	13
						T	3.26	10	0	451	7
PLd_{net}^{12}	–	12	20	–	–	A	1.02	8	2	1014	50
PLd_{net}^{14}	–	14	25	–	–	T	1.01	6	1	894	22

[^] SN = sharp-notch, BN = blunt-notch, PL = plain.

[#] distance between M6-screws for current supply (see Fig. 5).

[°] distance between M3-screws for potential drop measurement (see Fig. 5).

[*] A = axial, B = bending, T = torsion, B + T = combined bending-torsion, ϕ = shift-angle between bending and torsion stresses.

[+] high-cycle fatigue strength referred at a total fatigue life $N_A = 2 \cdot 10^6$ cycles and a survival probability 50%. $\Delta\sigma_A$ is valid for specimens tested under pure axial or pure bending loadings, while $\Delta\tau_A$ is valid for specimens tested under pure torsion or combined bending-torsion loadings.

[**] k is the inverse slope of the relevant Woehler curve fitted on total fatigue life data.

Axial tests have been performed by means of a servo-hydraulic MTS testing machine, with a load capacity of 250 kN and equipped with a MTS TestStar IIm controller. A sinusoidal load cycle was imposed under load control with a nominal load ratio R equal to -1 and a frequency f in the range 10–30 Hz, depending on the applied load level. The flexible test bench shown in Fig. 4 has been adopted to perform pure bending, pure torsion and combined bending-torsion fatigue tests. The tested specimens have been fixed to the bench by using friction grips clamped by four tightened bolts. One specimen’s extremity was fixed to a vertical support shown in Fig. 4c, the other one being bolted to a lever arm, that was loaded at its extremities by means of two independent servo-hydraulic actuators (Fig. 4a), equipped with 15 kN load cells and driven by a closed-loop digital controller MTS Flex Test 60. To allow for the arc-shaped trajectory of the lever arm extremities induced by the torsional and flexural compliance of the specimen, spherical jointshave been employed to connect each servo-hydraulic cylinder both to the lever arm and to its backing plate. A sinusoidal load cycle was imposed to each actuator, with a nominal load ratio R equal to −1 and a load frequency in the range 2–8 Hz, depending on the applied load level. Such reduced load frequencies were adopted in order to prevent the specimen slippage inside the grips.

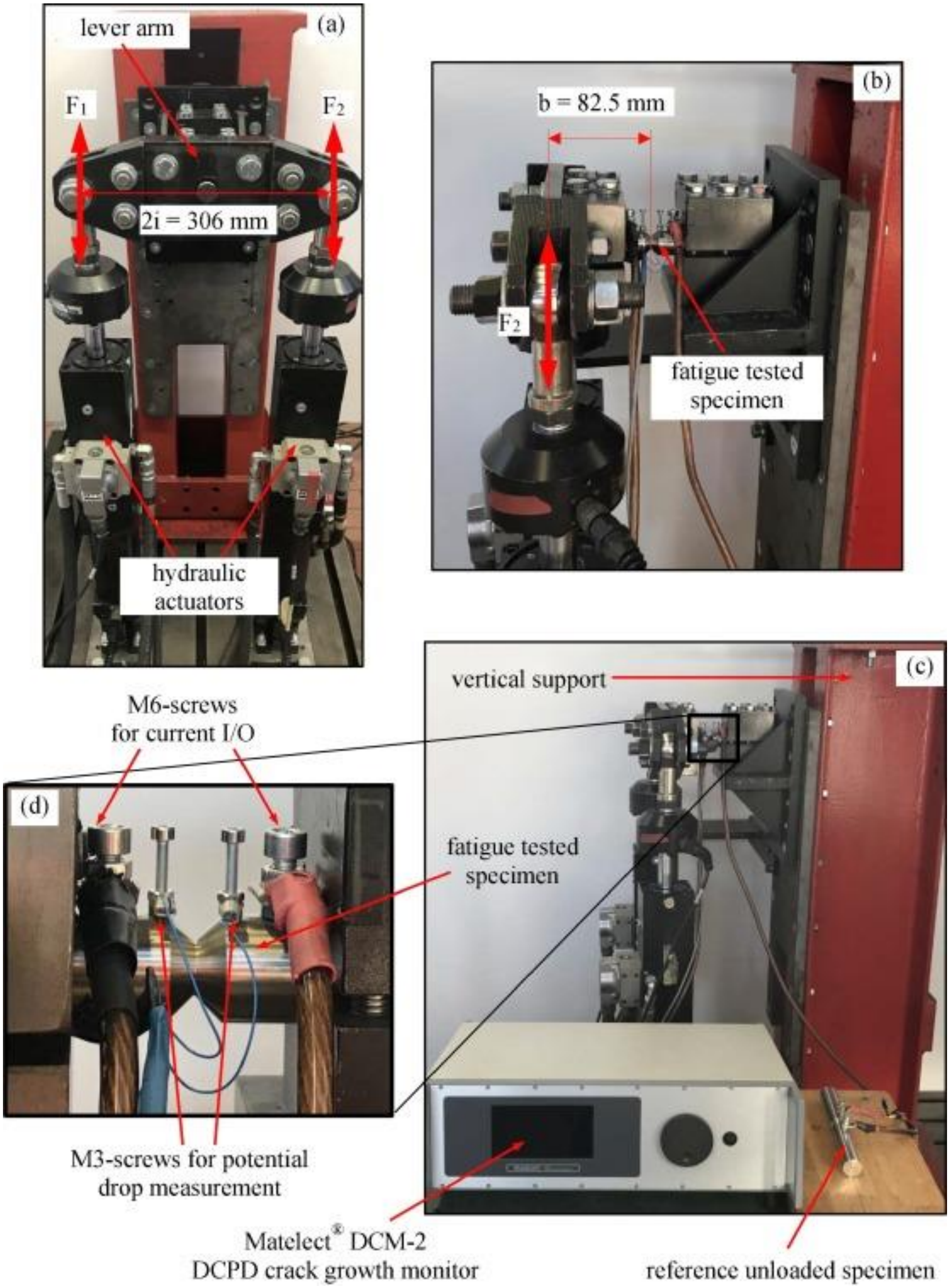

Fig. 4. Flexible test bench adopted for pure bending, pure torsion and combined bending-torsion fatigue tests. Definition of (a) torsion and (b) bending moment arms.

The Matelect® DCM-2 DCPD crack growthmonitor device with (c) the reference specimen and (d) the loaded one.

Dealing with combined bending-torsion fatigue tests, a stress-based biaxiality ratio τ_a/σ_aequal to √3 and a phase-shift ϕ equal to 0° or 90° have been adopted. The adopted τ_a/σ_aratio resulted in a SED-based biaxiality ratio $\Delta\overline{W}_{III}/\Delta\overline{W}_{I}$ equal to 2.43 and 6.18 in the case of sharp and blunt notched specimens, respectively.
Concerning axial tests, given the axial load F(t) applied to the specimen, the nominal normal stress in the net-section has been calculated from the following expression:

$$\sigma(t)=\frac{F(t)}{A_{net}}=\frac{F(t)}{\frac{\pi}{4}\cdot d_{net}^2} \tag{10}$$

Concerning pure bending, pure torsion and combined bending-torsion fatigue loadings the external loads F_1 and F_2 exerted by the hydraulic actuators according to Fig. 4 resulted in bending and torsion moments at the specimen net-section as follows:

$$M_b(t)=[F_1(t)+F_2(t)]\cdot b \tag{11a}$$

$$M_t(t)=[F_1(t)-F_2(t)]\cdot i \tag{11b}$$

where b and i are the bending and torsion moment arms, respectively, while F_1 and F_2 are the loads applied by the actuators, as reported in Fig. 4a and b. The nominal bending and torsion stresses at the specimen net-section can be expressed as:

$$\sigma(t)=\frac{M_b(t)}{W_b} \tag{12a}$$

$$\tau(t)=\frac{M_t(t)}{W_t} \tag{12b}$$

W_b and W_t being the section moduli defined as:

$$W_b=\frac{\pi}{32}\cdot d_{net}^3 \tag{13a}$$

$$W_t=\frac{\pi}{16}\cdot d_{net}^3 \tag{13b}$$

By taking advantage of Eqs. (11a), (11b), (12a), (12b), the external loads F_1 and F_2 to apply can be derived as functions of desired values of bending and torsion net-section stress amplitudes, σ_a and τ_a, respectively. By considering a nominal load ratio R = −1, i.e. mean stresses equal to zero, and the most general case of a phase-shift ϕ ≠ 0 between torsion and bending stress components, the loads F_1 and F_2 result as follows (see also [59] for more general expressions):

$$\begin{aligned} F_1(t)&=\frac{1}{2}\frac{W_b}{b}\sigma(t)+\frac{W_t}{i}\tau(t)=\frac{1}{2}\frac{W_b}{b}\sigma_a\cdot\sin(2\pi ft)+\frac{W_t}{i}\tau_a\cdot\sin(2\pi ft+\phi)\\ F_2(t)&=\frac{1}{2}\frac{W_b}{b}\sigma(t)-\frac{W_t}{i}\tau(t)=\frac{1}{2}\frac{W_b}{b}\sigma_a\cdot\sin(2\pi ft)-\frac{W_t}{i}\tau_a\cdot\sin(2\pi ft+\phi)\end{aligned} \tag{14}$$

Previous Eq. (14) gives as master cases:

(15a)$F1(t)=12Wbb\sigma a+Wti\tau a\cdot\sin(2\pi ft)F2(t)=12Wbb\sigma a-Wti\tau a\cdot\sin(2\pi ft)if\phi=0$(in-phase)

(15b)$F1(t)=12Wbb\sigma a2+Wti\tau a2\cdot\sin(2\pi ft+\gamma)F2(t)=12Wbb\sigma a2+Wti\tau a2\cdot\sin(2\pi ft-\gamma)if\phi=90°$(out-of-phase)

where f is the load frequency, while γ, defined by Eq. (16), is the phase-shift between the loads applied by the actuators, which in principle can be different from the desired phase-shift ϕ between bending and torsion stress components.

(16)$\gamma=\arcsin Wti\tau aWbb\sigma a2+Wti\tau a2$

Before initiating the test campaign, the bending and torsion stresses to apply have been successfully assessed in all loading cases (B, T, B + T ϕ = 0°, B + T ϕ = 90°) by using a −45°/0°/45° strain gauge rosette glued on a dedicated test specimen. All fatigue tests have been interrupted at the complete stiffness loss. Run out condition has been assumed at $2\cdot10^6$ cycles for axial fatigue tests, and at approximately 10^6 cycles for multiaxial tests, given the reduced load frequency.

In fatigue tests of notched specimens, the fatigue crack initiation and propagation phases have been monitored by using the Matelect® DCM-2 direct current potential drop (DCPD) method, as shown in Fig. 4c and d. The experimental set-up of the DCPD measurement chain is sketched in Fig. 5.

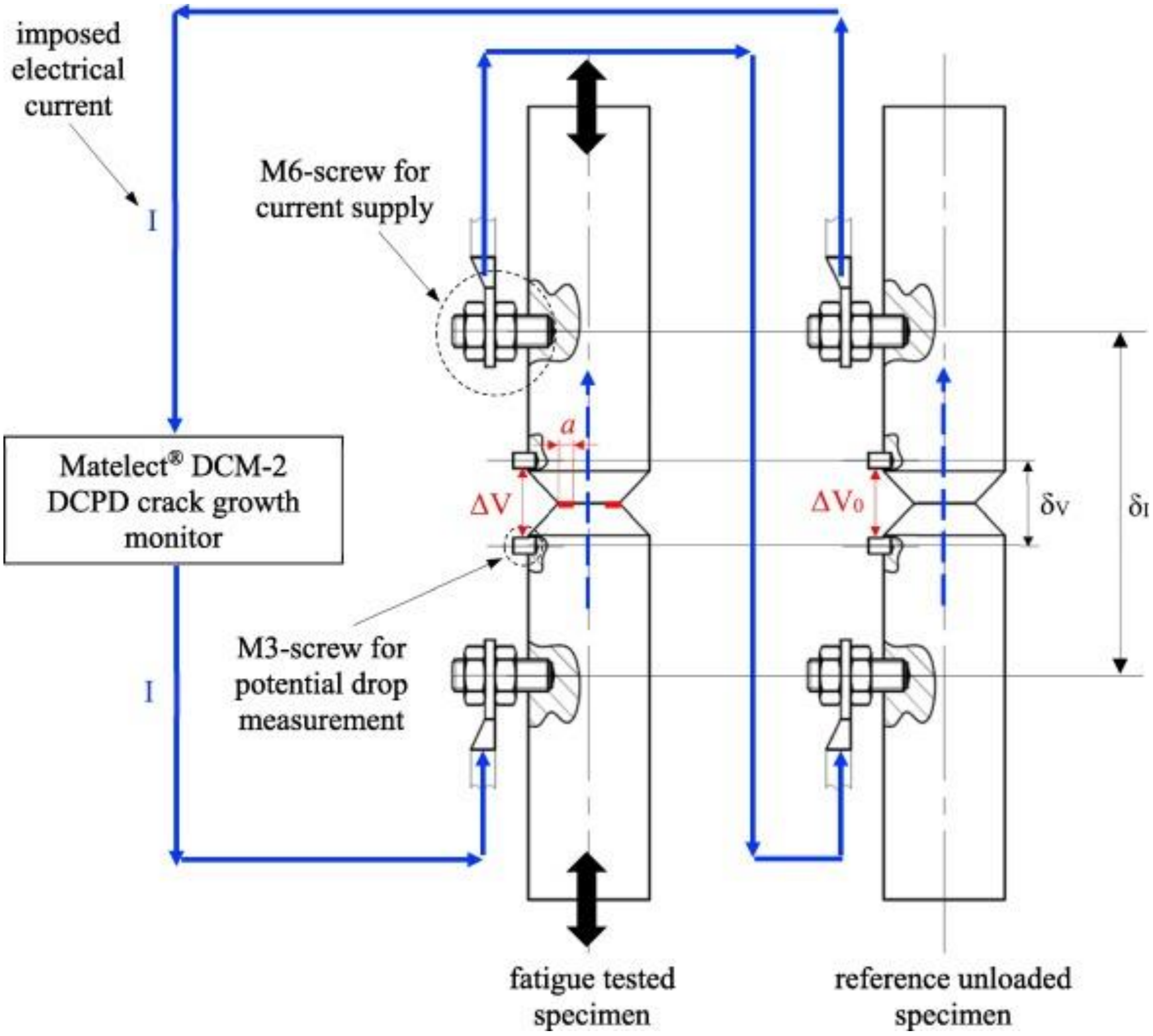

Fig. 5. Experimental setup of the electrical potential drop measurement system; δ_I and δ_V are the distances between the points for current supply and potential drop measurement, respectively.

The adopted DCPD technique uses two specimens in order to compensate thermal effects: one is the fatigue tested specimen, while the other one is the reference unloaded specimen (see Fig. 4c and d). The two samples have been connected in series and a constant 30 A current (I in Fig. 5) flowed through both of them, the supply cables being connected to each specimen by means of M6 screws located at a distance δ_I from each other (see Fig. 5 and Table 3). During each fatigue test, the potential drops ΔV, relevant to the loaded specimen, and ΔV_0, relevant to the reference unloaded one, were measured by means of signal cablesfixed with two M3 screws close to the notch edges at a distance δ_V from each other (see Fig. 5 and Table 3). The sampling rate was set in the range 1/200–1/100 times the load frequency f. In plain specimens the adopted DCPD equipment did not appreciate any crack initiation phenomenon preceding the final fracture. Therefore, the DPCD method has not been applied to plain specimens.

4. Fatigue test results

4.1. Analysis of fracture surfaces

Fig. 6 reports typical fracture surfaces of notched specimens subjected to different uniaxial and multiaxial loading conditions. The results shown are relevant to the medium or high-cycle fatigue regimes.

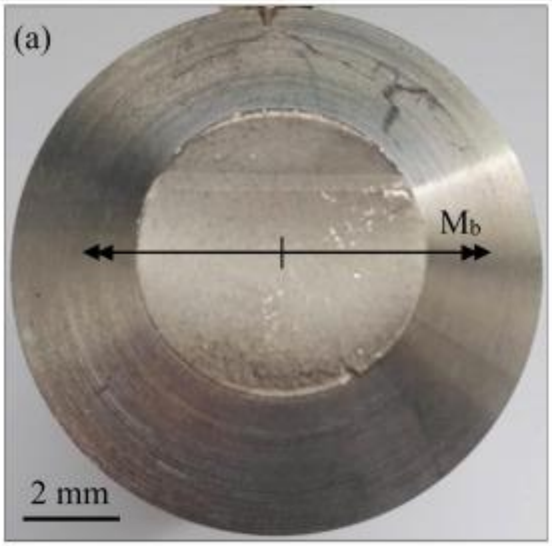

SN_ρ0.1_d_{net}12
pure bending, $\Delta\sigma$=389 MPa, N_f=300707

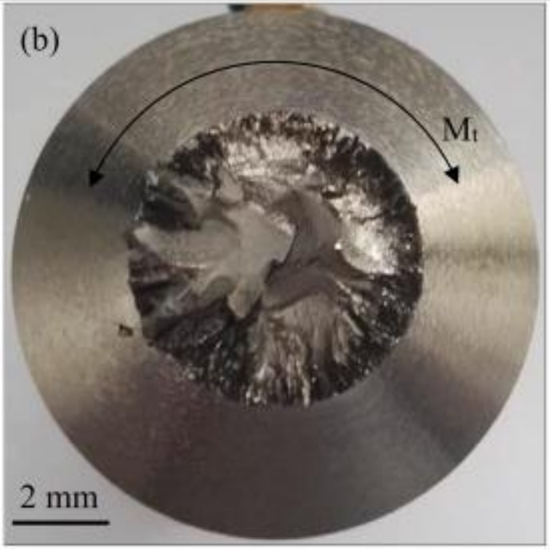

SN_ρ0.1_d_{net}12
pure torsion, $\Delta\tau$=631 MPa, N_f=501363

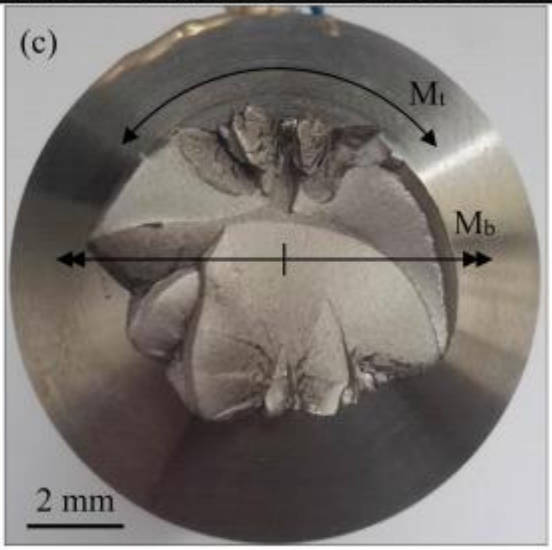

SN_ρ0.1_d_{net}12
bending-torsion, ϕ=0, $\Delta\sigma$=255 MPa, $\Delta\tau$=442 MPa, N_f=439682

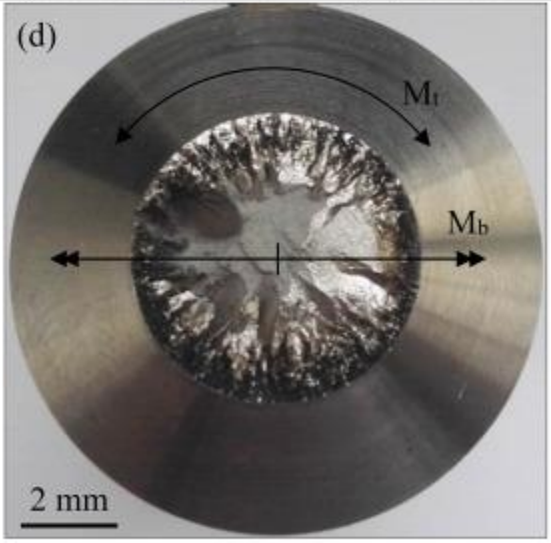

SN_ρ0.1_d_{net}12
bending-torsion, ϕ=90, $\Delta\sigma$=289 MPa,$\Delta\tau$=501 MPa, N_f=214538

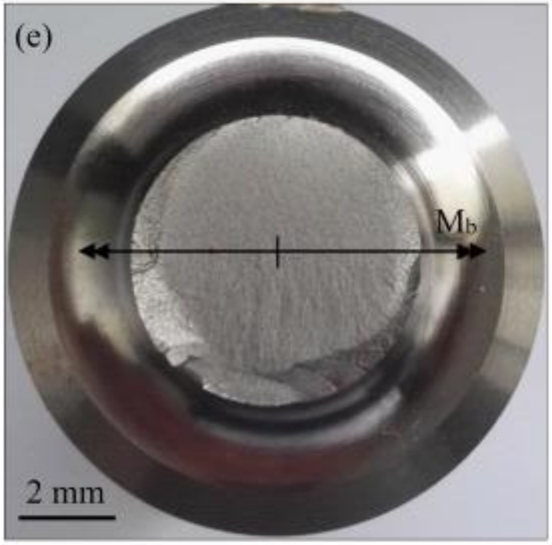

BN_ρ4_d_{net}12
pure bending, $\Delta\sigma$=1167 MPa, N_f=54872

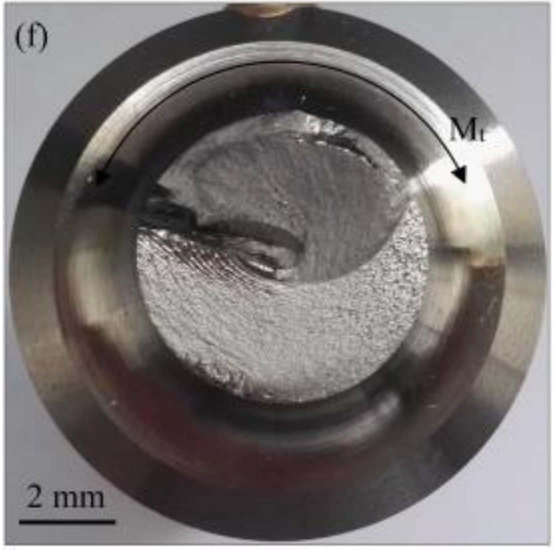

BN_ρ4_d_{net}12
pure torsion, $\Delta\tau$=884 MPa, N_f=239926

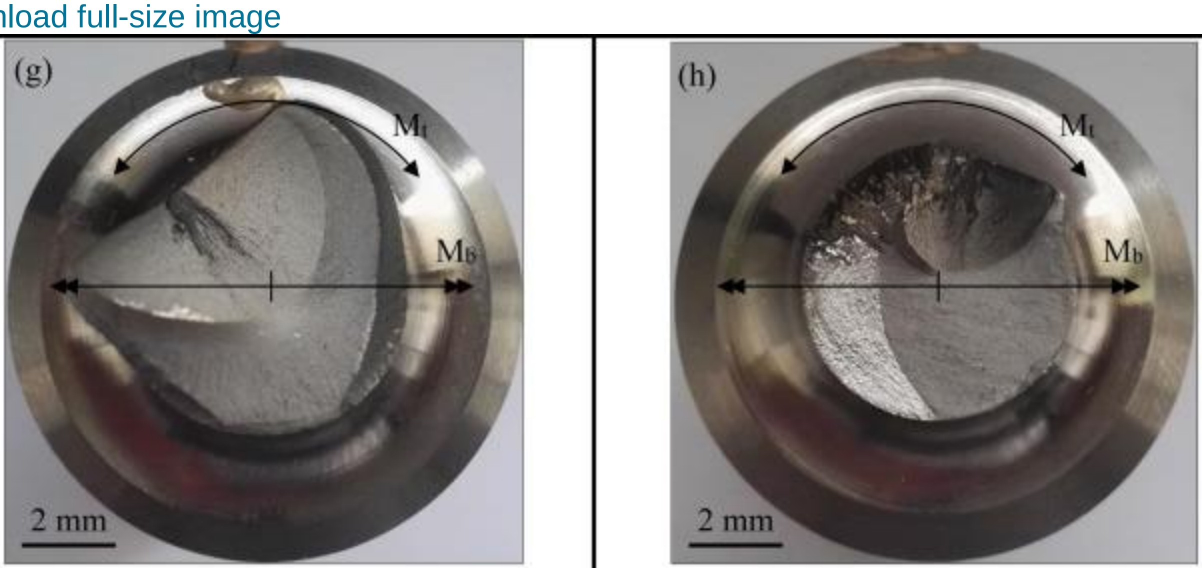

BN_ρ4_d_{net}12
bending-torsion, $\phi=0$, $\Delta\sigma=462$ MPa, $\Delta\tau=800$ MPa, $N_f=123732$

BN_ρ4_d_{net}12
bending-torsion, $\phi=90$, $\Delta\sigma=416$ MPa, $\Delta\tau=721$ MPa, $N_f=483924$

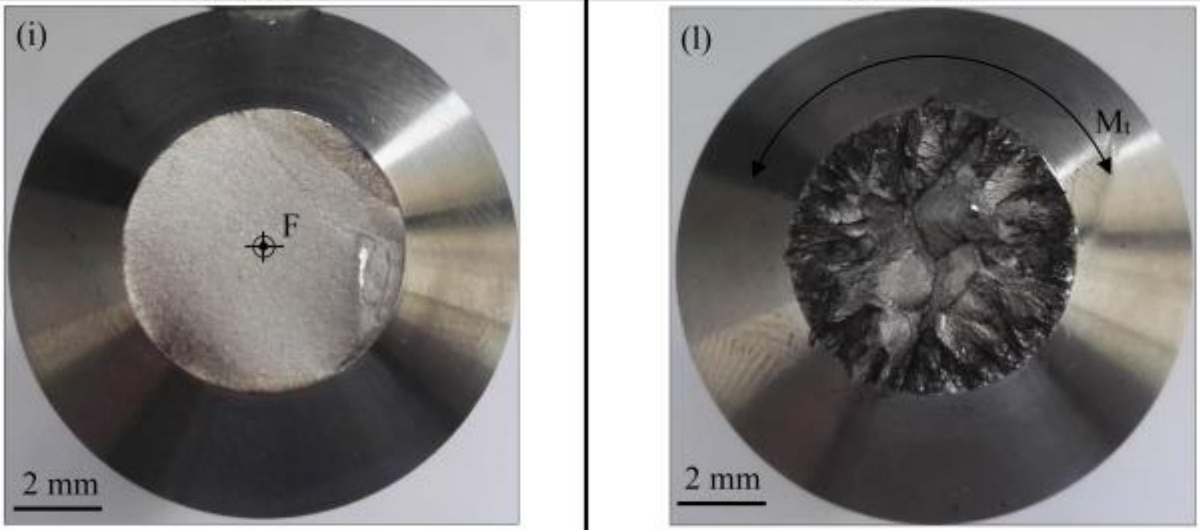

SN_ρ0.1_d_{net}13
pure axial, $\Delta\sigma=256$ MPa, $N_f=771063$

SN_ρ0.1_d_{net}13
pure torsion, $\Delta\tau=525$ MPa, $N_f=828384$

Fig. 6. Fracture surfaces of sharply V-notched specimens under (a) pure bending, (b) pure torsion, (c) in-phase bending-torsion and (d) out-of-phase bending-torsion; of bluntly notched specimens under (e) pure bending, (f) pure torsion, (g) in-phase bending-torsion and (h) out-of-phase bending torsion; and of sharply V-notched specimens under (i) pure axial and (l) pure torsion fatigue loadings.

It can be observed that under pure bending or pure axial fatigue loadings of sharply and bluntly notched specimens (Fig. 6a, e, i), almost flat fracture surfaces have been obtained, due to the initiation and subsequent propagation of semi-elliptical, pure mode I cracks propagating in the net-section area. In the case of bending loading (Fig. 6a and e), the crack always initiated from the maximum bending stress regions, while under axial loading (Fig. 6i) multiple crack initiation points were observed at different angular positions along the notch tip.

In the case of pure torsion or combined bending-torsion loadings of all notched specimens (Fig. 6b–d, f–h, l), again multiple crack initiation points along the notch tip profile were noted. Dealing with sharp V-notches (Fig. 6b–d, l), crack paths gave rise to the fracture surface morphology known as factory-roof. Under pure torsion or out-of-phase bending-torsion loadings (Fig. 6b, d, l), resulting factory-roofs were characterized by a reduced height, their peaks having been smoothed and polished during fatigue testing by the sliding contact, friction and meshing between crack surfaces. As a result, a lot of powder and debris were emanated from the notch tip, as highlighted in Fig. 7. On the other hand, under in-phase bending-torsion loadings (Fig. 6c), no powder has been observed at the notch tip and the obtained factory-roofs were more pronounced and distinguishable. Dealing with blunt notches (Fig. 6f–h), almost flat fracture surfaces were obtained under torsion or out-of-phase bending-torsion loadings (Fig. 6f and h), while more complex fracture surface morphologies have been obtained under in-phase bending-torsion loadings (Fig. 6g), since crack propagation occurred also out of the net-section within the notch mouth. As compared to sharp V-notches, factory-roofs and powder emanating from the notch tip were almost completely absent.

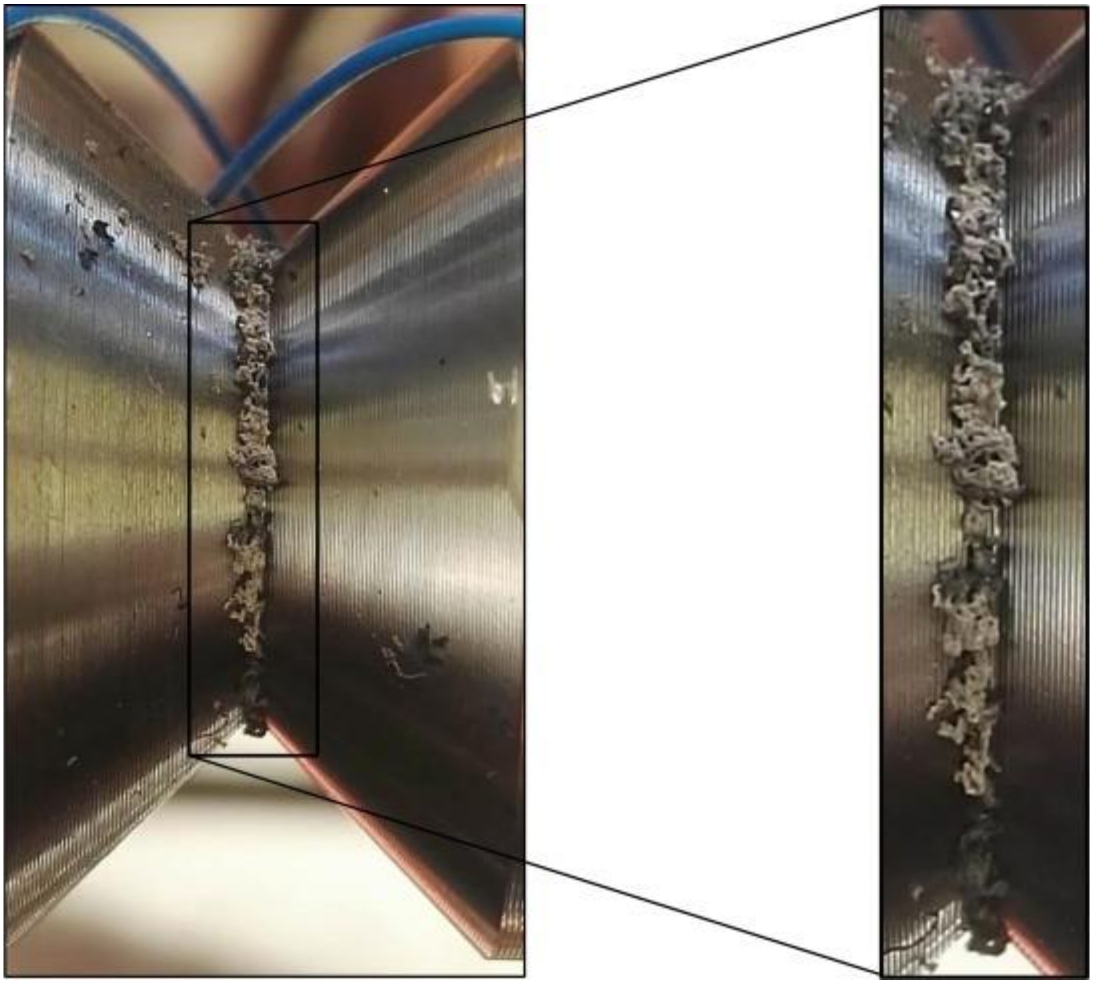

1. Download high-res image (394KB)
2. Download full-size image

Fig. 7. Powder and debris emanated during crack propagation from the notch tip of a sharp V-notched specimen under pure torsion loading, due to sliding contact, friction and meshing between crack surfaces.

Fig. 8a and b report two examples of fracture surfaces obtained by fatigue testing plain specimens under pure axial and pure torsion loading, respectively. Under axial loading (Fig. 8a), a fatigue crack initiated and then propagated in the net-section under pure mode I loading with a semi-elliptical shape, until fracture occurred. Under torsion loading (Fig. 8b and c), multiple cracks initiated along the longitudinal direction (Fig. 8c) on a plane of maximum shear stress, then crack branching occurred causing the previously parallel cracks to coalesce; eventually the subsequent crack propagation generated almost flat fracture surfaces, where the material was completely smeared (Fig. 8b).

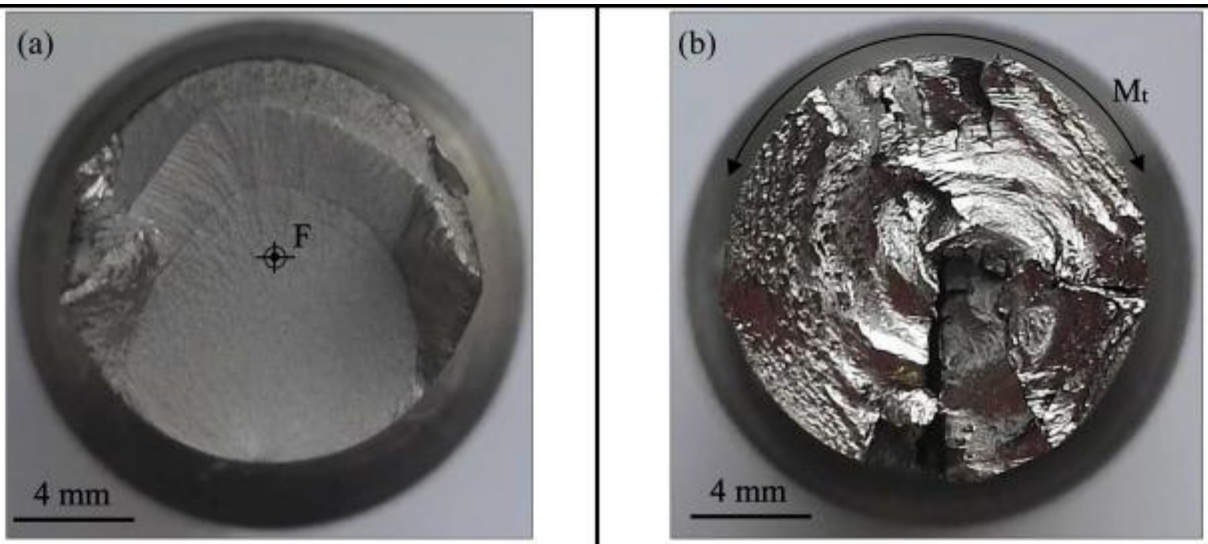

PL_d_{net}12
pure axial, $\Delta\sigma$=1078 MPa, N_f=106083

PL_d_{net}14
pure torsion, $\Delta\tau$=1060 MPa, N_f=69300

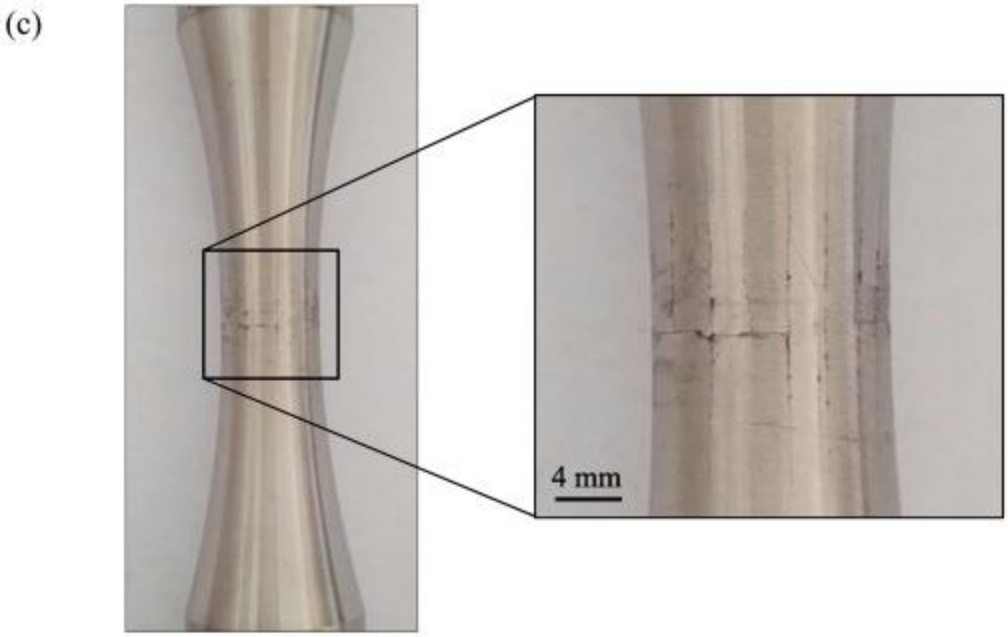

PL_d_{net}14, pure torsion, $\Delta\tau$=954 MPa, N_f=420971

Fig. 8. Fracture surfaces of plain specimens under (a) pure axial loading, and (b) pure torsion fatigue loading. (c) Multiple cracks initiated and propagated along the longitudinal direction of a plain specimen under pure torsion loading.

4.2. Analysis of DCPD signals

Fig. 9 reports some typical potential drops signals, $\Delta V/\Delta V_0$ (see Fig. 5), as a function of the number of loading cycles, for each specimen geometry and applied loading conditions. It would be possible to define a technical fatigue crack initiation life at a fixed increase of the potential drop $\Delta V/\Delta V_0$, for example equal to 1%, as adopted by Tanaka in a recent contribution [11]. However, the definition of crack initiation life N_i correlated to a fixed crack depth, rather than to a fixed increase of the potential drop $\Delta V/\Delta V_0$, has been investigated here, as it will be discussed later on when commenting on Fig. 15.

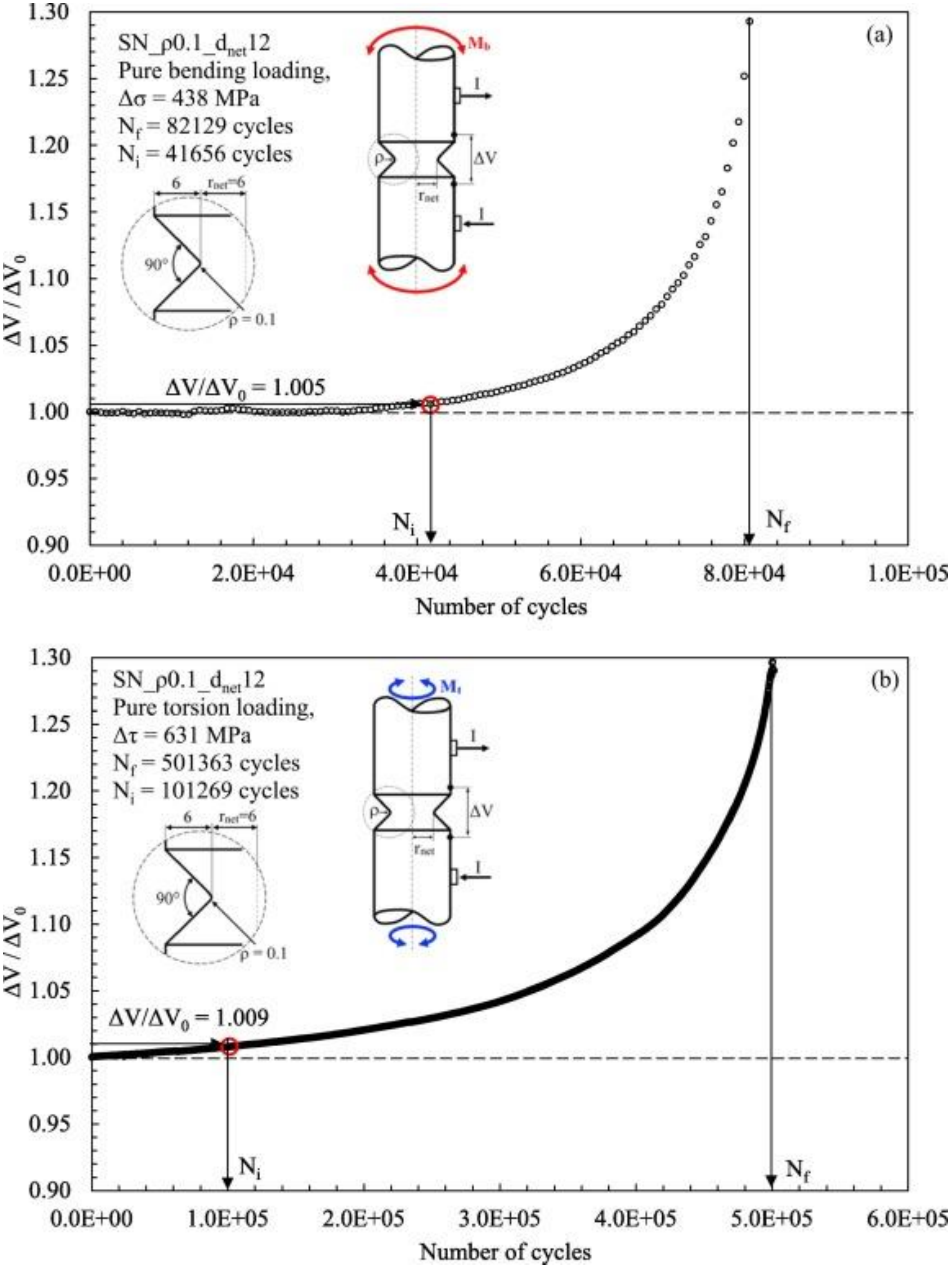
(a)
SN_ρ0.1_dnet12
Pure bending loading,
Δσ = 438 MPa
Nf = 82129 cycles
Ni = 41656 cycles
6
rnet=6
90°
ρ = 0.1
Mb
I
ΔV
ρ
rnet
ΔV/ΔV0 = 1.005
Ni
Nf
ΔV / ΔV0
1.30
1.25
1.20
1.15
1.10
1.05
1.00
0.95
0.90
0.0E+00
2.0E+04
4.0E+04
6.0E+04
8.0E+04
1.0E+05
Number of cycles
(b)
SN_ρ0.1_dnet12
Pure torsion loading,
Δτ = 631 MPa
Nf = 501363 cycles
Ni = 101269 cycles
6
rnet=6
90°
ρ = 0.1
Mt
I
ΔV
ρ
rnet
ΔV/ΔV0 = 1.009
Ni
Nf
ΔV / ΔV0
1.30
1.25
1.20
1.15
1.10
1.05
1.00
0.95
0.90
0.0E+00
1.0E+05
2.0E+05
3.0E+05
4.0E+05
5.0E+05
6.0E+05
Number of cycles

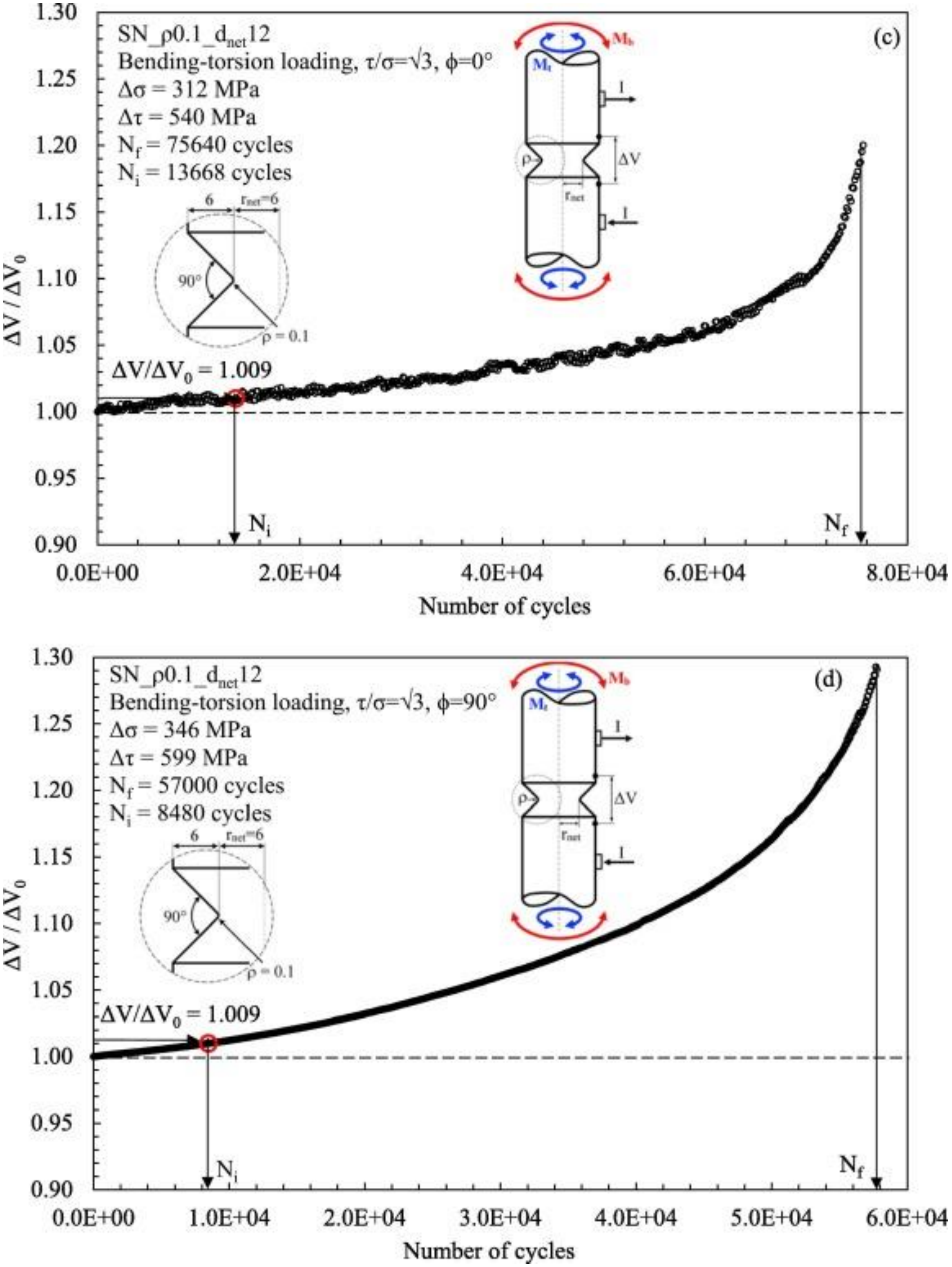

1. Download high-res image (595KB)
2. Download full-size image

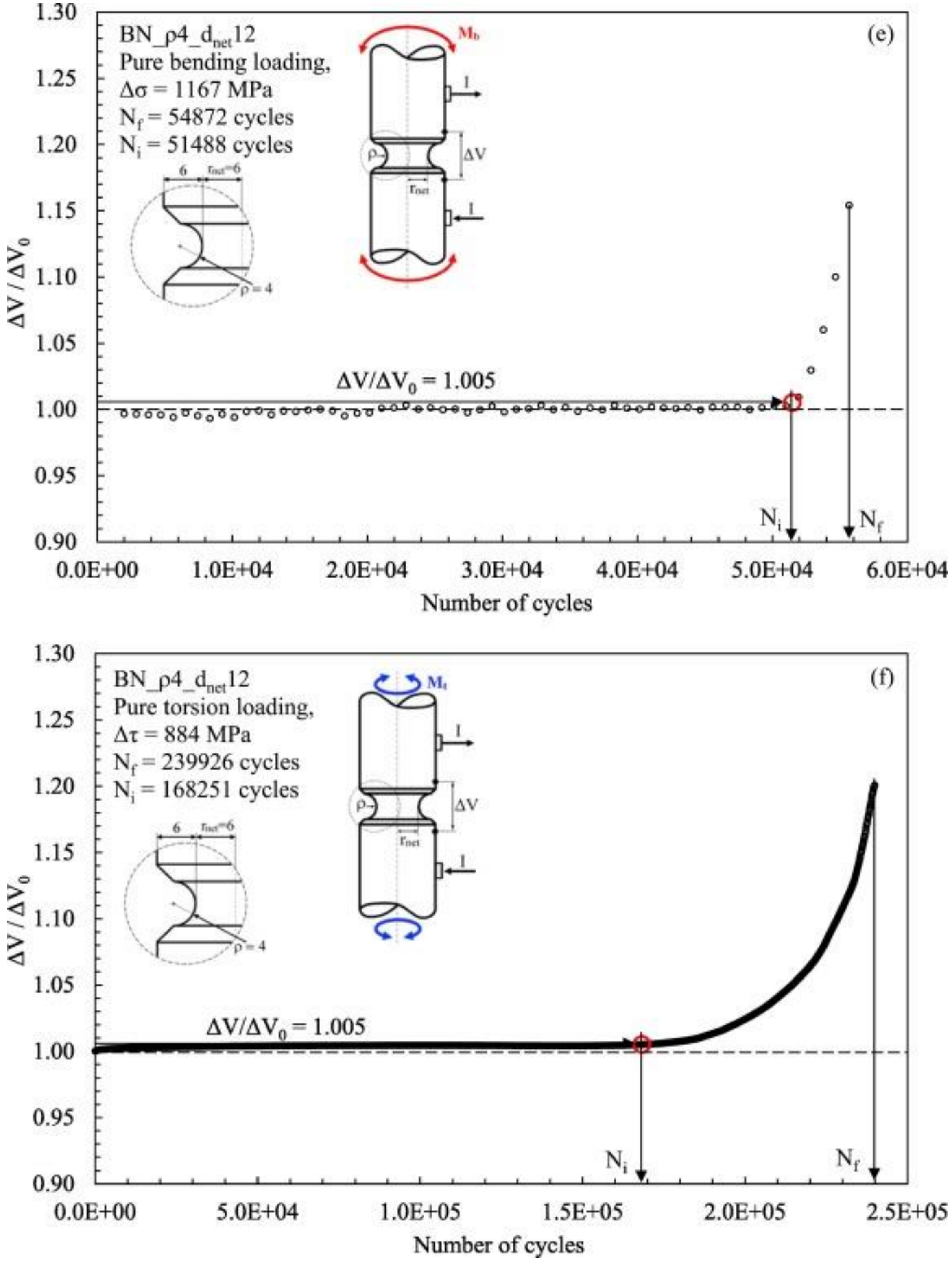
BN_ρ4_dnet12
Pure bending loading,
Δσ = 1167 MPa
Nf = 54872 cycles
Ni = 51488 cycles
(e)
Mb
ΔV
ρ
rnet
6
rnet=6
ρ = 4
ΔV/ΔV0 = 1.005
Ni
Nf
ΔV / ΔV0
1.30
1.25
1.20
1.15
1.10
1.05
1.00
0.95
0.90
0.0E+00
1.0E+04
2.0E+04
3.0E+04
4.0E+04
5.0E+04
6.0E+04
Number of cycles
BN_ρ4_dnet12
Pure torsion loading,
Δτ = 884 MPa
Nf = 239926 cycles
Ni = 168251 cycles
(f)
Mt
ΔV
ρ
rnet
6
rnet=6
ρ = 4
ΔV/ΔV0 = 1.005
Ni
Nf
ΔV / ΔV0
1.30
1.25
1.20
1.15
1.10
1.05
1.00
0.95
0.90
0.0E+00
5.0E+04
1.0E+05
1.5E+05
2.0E+05
2.5E+05
Number of cycles

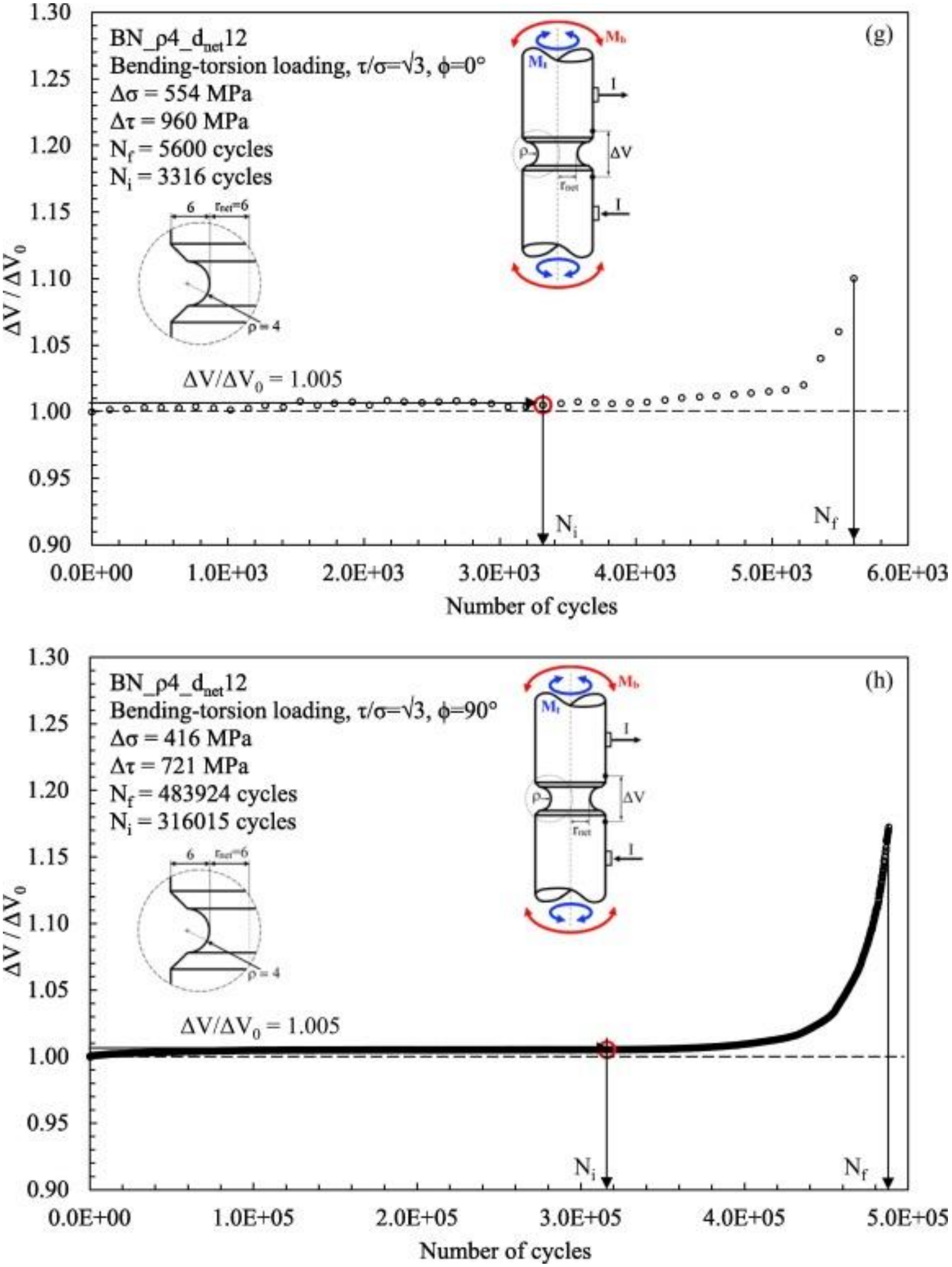

Fig. 9. Potential drop measured during fatigue tests of sharp and blunt notches under (a, e) pure bending, (b, f) pure torsion, (c, g) in-phase bending-torsion and (d, h) out-of-

phase bending-torsion. N_f is the total fatigue life, while N_i is the crack initiation life defined according to next Fig. 15.

Dealing with sharp V-notches, it can be observed that under pure bending loading (Fig. 9a) the ratio between crack initiation life, N_i, and total fatigue life, N_f, is approximately equal to 50–60%, so that the fatigue life spent to initiate the crack almost equals that spent to propagate it. On the other hand, under pure torsion or combined bending-torsion loadings (Fig. 9b–d), the initiation life covers only a small portion of the total life (about 10–20%), so that the fatigue life is mainly spent for crack propagation. Approximately the same initiation-to-total life ratio can be observed under in-phase and out-of-phase multiaxial loadings (see Fig. 9c and d in comparison).
Concerning blunt notches, different results have been obtained, an higher ratio N_i/N_f having been observed under all loading conditions: under pure bending (Fig. 9e) the ratio N_i/N_f is around 90–95%, while under pure torsion or combined bending-torsion loadings the ratio N_i/N_f is about 60–70% (Fig. 9f–h). Again, the phase shift between bending and torsion does not alter significantly the initiation-to-total life ratio (see Fig. 9g and h in comparison).

4.3. Woehler curves

The experimental fatigue results expressed in terms of the applied nominal net-section stress range (defined as maximum value minus minimum value) have been reported for all tested specimens in Fig. 10a and b in terms of total fatigue life N_f and crack initiation life N_i, respectively. Even if the latter has been defined according to next Fig. 15 and will be discussed later on, nevertheless crack initiation data have been reported here for comparison purposes. It should be noted that for specimens tested under pure axial or pure bending fatigue loadings, the normal stress range $\Delta\sigma$ (defined as maximum value minus minimum value) evaluated by means of Eqs. (10), (12a), respectively, has been reported in Fig. 10a and b, while for specimens tested under pure torsion or combined bending-torsion loadings, the shear stress range $\Delta\tau$ evaluated by means of Eq. (12b) has been adopted for data representation.

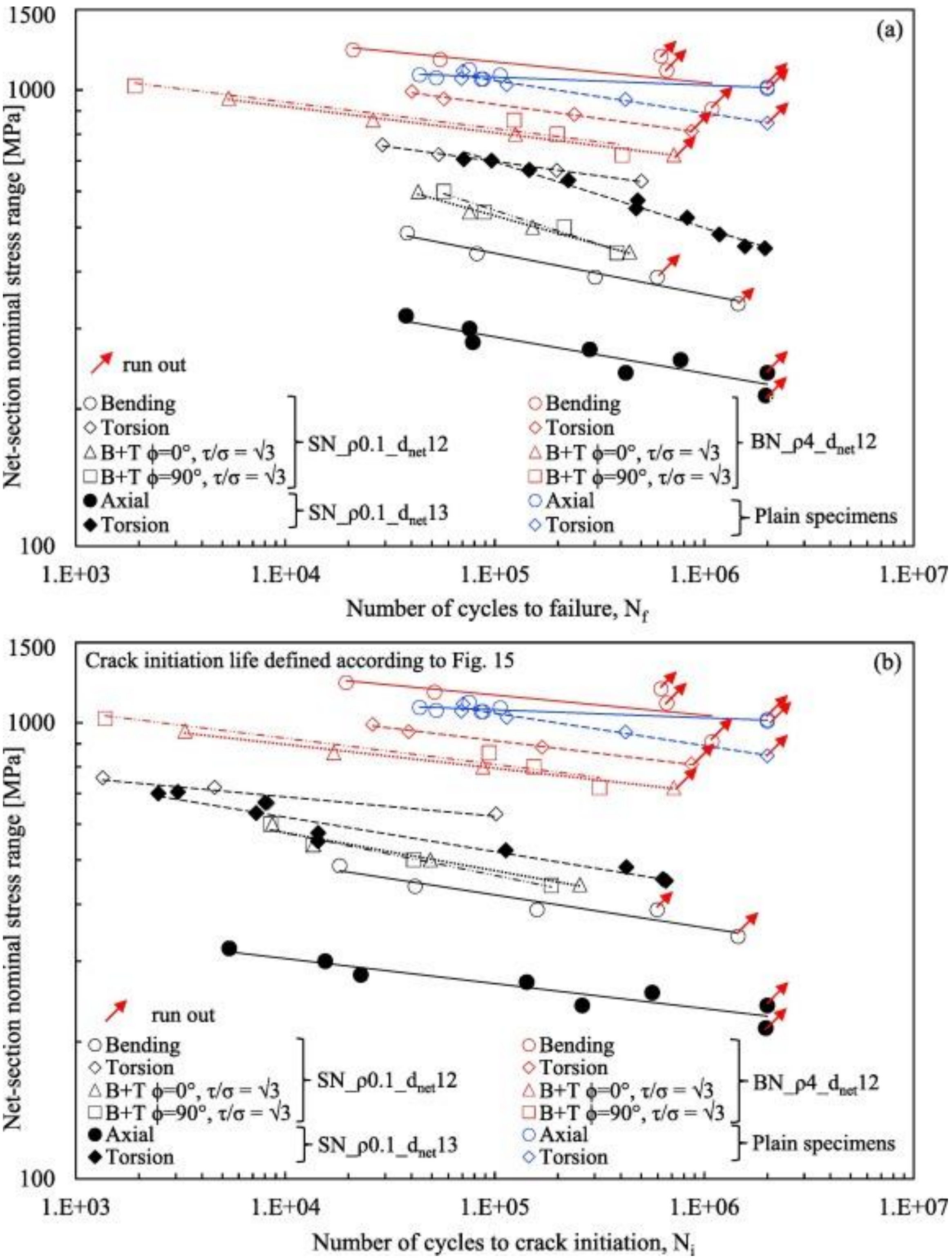

Fig. 10. Experimental fatigue results expressed in terms of applied nominal net-section stress range and (a) total fatigue life and (b) crack initiation life (defined

according to next Fig. 15). The nominal net-section stress range equals Δσ for specimens tested under pure axial (Eq. (10)) or pure bending (Eq. (12a)) loadings, while it equals Δτ (Eq. (12b)) for specimens tested under pure torsion or combined bending-torsion loadings.

A statistical re-analysis has not been performed for each specimen geometry and loading condition, due to the reduced number of experimental data for each data series (see also summary in Table 3). However, in order to improve the readability of the data, a fitting curvehas been included in Fig. 10a and b for each data series. It can be observed that the inverse slope k of the fitting curves results very flat especially for plain and blunt notched specimens ($16 < k < 50$), while it results steeper for sharp notched specimens ($7 < k < 16$).

Interestingly, Fig. 10b shows that sharp notches exhibit higher fatigue strength under pure torsion as compared to pure bending loading. Conversely, blunt notches are weaker under pure torsion than under pure bending. As expected, in sharp notches subjected to pure torsion the crack initiation plane is normal to the specimen's longitudinal axis, conversely it was noted that in blunt notches the crack initiation plane is primarily its reciprocal, i.e. in the plane parallel to the specimen's longitudinal axis, as it was previously shown in Fig. 8c for plain specimens. While in sharp notches, initiation is forced in the plane normal to the specimen's axis, in blunt notches the plane parallel to the specimen's axis is fully active to initiate a crack. The material resistance to shear stresses being weaker in this plane, as Fig. 8c demonstrate, it is the actual crack initiation plane. The difference of sharp and blunt notches in terms of material cracking behavior under pure torsion suggests an explanation for their different relative fatigue strength with specimens of the same geometry but subject to pure bending.

Moreover, it should be noted that the notch-strengthening phenomenon under pure torsion or combined bending and torsion has not been found in the considered titanium alloy, since at a given net-section stress amplitude the higher the stress concentration factor, the shorter the fatigue life.

Finally, on the basis of the obtained results, no influence of the phase-shift between bending and torsion stresses can be observed on the fatigue strength of the considered titanium alloy. This observation is valid for either sharp or blunt notches and for total as well as crack initiation life. Similar results were previously obtained in [47] by fatigue testing sharp V-notched specimens under combined axial-torsion loading on the same material. This is quite in good agreement with Fatemi et al. [60] and Fatemi and

Shamsaei [61], who observed only a limited detrimental effect of the phase-shift by fatigue testing thin-walled tubular specimens made of Ti-6Al-4V and plain specimens made of Ti-6.5Al-3.4Mo, respectively, under combined axial-torsion loading. Therefore, the original formulation of the SED approach as proposed by Lazzarin and collaborators [9], which does not account for the phase-shift between the different loadings, seems to be well applicable to the present experimental fatigue data.

5. The SED approach applied to crack initiation data

5.1. The structural volume size under pure axial and pure torsion fatigue

To calculate the control radii $R_{0,I}$ and $R_{0,III}$ by means of Eqs. (6), (7), the experimental fatigue results generated from geometries (b), (c) and (d) of Fig. 3 have been selected from previous Fig. 10a and reported in Fig. 11a and b. They include plain and sharp V-notched specimens under pure axial (mode I, Fig. 11a) and pure torsion (mode III, Fig. 11b) loadings.

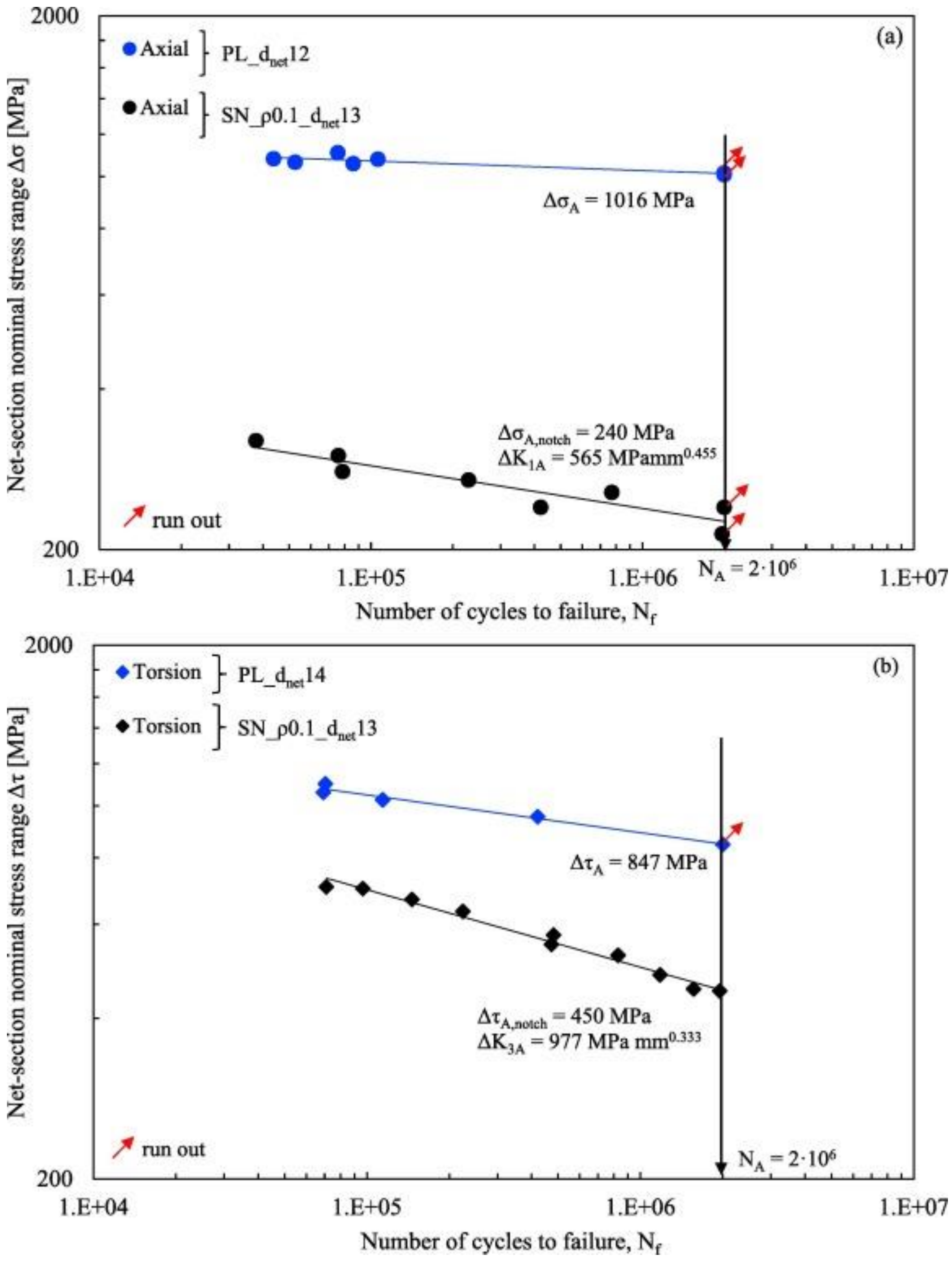

Fig. 11. Experimental fatigue results adopted to define the control radii $R_{0,I}$ (Eq. (6)) and $R_{0,III}$ (Eq. (7)) for the averaged SED calculation. Test data are expressed in terms of the

applied nominal net-section stress range and are relevant to plain and sharp V-notched specimens tested under (a) pure axial and (b) pure torsion loadings.

The material fatigue limits and the threshold values of the NSIFs range appearing in Eqs. (6), (7) have been substituted with the high-cycle fatigue strengths at $N_A = 2 \cdot 10^6$ cycles. The high-cycle fatigue strengths of plain specimens subjected to pure axial and pure torsion loadings resulted $\Delta\sigma_A = 1016$ MPa and $\Delta\tau_A = 847$ MPa, respectively. Regarding sharp V-notched specimens, the NSIF ranges, ΔK_1 and ΔK_3, for pure axial and pure torsion, respectively, have been derived by applying the Gross and Mendelson definitions [44], (8a), (8b), to the numerical results of dedicated FE analyses carried out by adopting very refined meshes close to the V-notch tip (element size on the order of 10^{-5} mm). The details of the FE analyses are not reported here for sake of brevity. The results of the dedicated FE analyses gave the following results:

$$(17a)\quad \Delta K_1 = 2.355\,\mathrm{mm}^{0.455} \cdot \Delta\sigma_{notch}$$

$$(17b)\quad \Delta K_3 = 2.170\,\mathrm{mm}^{0.333} \cdot \Delta\tau_{notch}$$

By substituting the high-cycle fatigue strengths of sharp V-notched specimens, i.e. $\Delta\sigma_{A,notch} = 240$ MPa and $\Delta\tau_{A,notch} = 450$ MPa (see Fig. 11a and b), the characteristic NSIF ranges are $\Delta K_{1,A} = 565$ MPa·mm$^{0.455}$ and $\Delta K_{3,A} = 977$ MPa·mm$^{0.333}$, respectively. Finally, by substituting the experimental values ($\Delta\sigma_A$, $\Delta K_{1,A}$) and ($\Delta\tau_A$, $\Delta K_{3,A}$) into Eqs. (6), (7), respectively, with $\lambda_1 = 0.544$, $\lambda_3 = 0.666$, $e_1 = 0.145$ and $e_3 = 0.310$ (from [18], [31], being $2\alpha = 90°$ and $\nu = 0.30$), the control radii resulted $R_{0,I} = 0.071$ mm and $R_{0,III} = 0.18$ mm.
To apply the physical definition of crack initiation (i.e. a physical crack *a* equal to R_0) by taking advantage of the DCPD method, the potential drop change $\Delta V/\Delta V_0$ has to be correlated with the crack depth *a* by means of proper calibration analyses.

5.2. Calibration curves of the direct current potential drop (DCPD) method

In their pioneering contributions [62], [63], Ritchie and co-workers showed that the calibration curves of the electrical potential drop method describing the potential drop $\Delta V/\Delta V_0$ versus the crack depth *a* for a specific specimen geometry and crack shape, can be accurately derived by means of finite element analyses, which are less complex than analytical calibrations and less time-consuming than experimental ones. In the present paper, the calibration curves have been calculated by means of electrical FE analyses by considering the notched specimen geometries reported in Fig. 3a and b. All FE analyses have been performed by using Ansys® software and by adopting a 3D, 10-node, tetrahedral, electric solid element (SOLID 232 of Ansys® element library).

Since it has been demonstrated in [64] that the potential drop calculated far from the notch tip is almost insensitive to the element size, rather coarse mesh patterns have been employed (see Fig. 12). Only one quarter of each specimen has been modelled, taking advantage of the symmetry on the XY plane and of the anti-symmetry on the specimen net-section, which translates in an electrical potential equal to 0 V applied to the un-cracked portion of the net-section area, to properly model the absence of electric contact between crack surfaces. Moreover, to simulate the operating conditions of the Matelect® DCM-2, a constant current $I = 30$ A has been applied to the FE models at the surface of the lower screw (see Fig. 12).

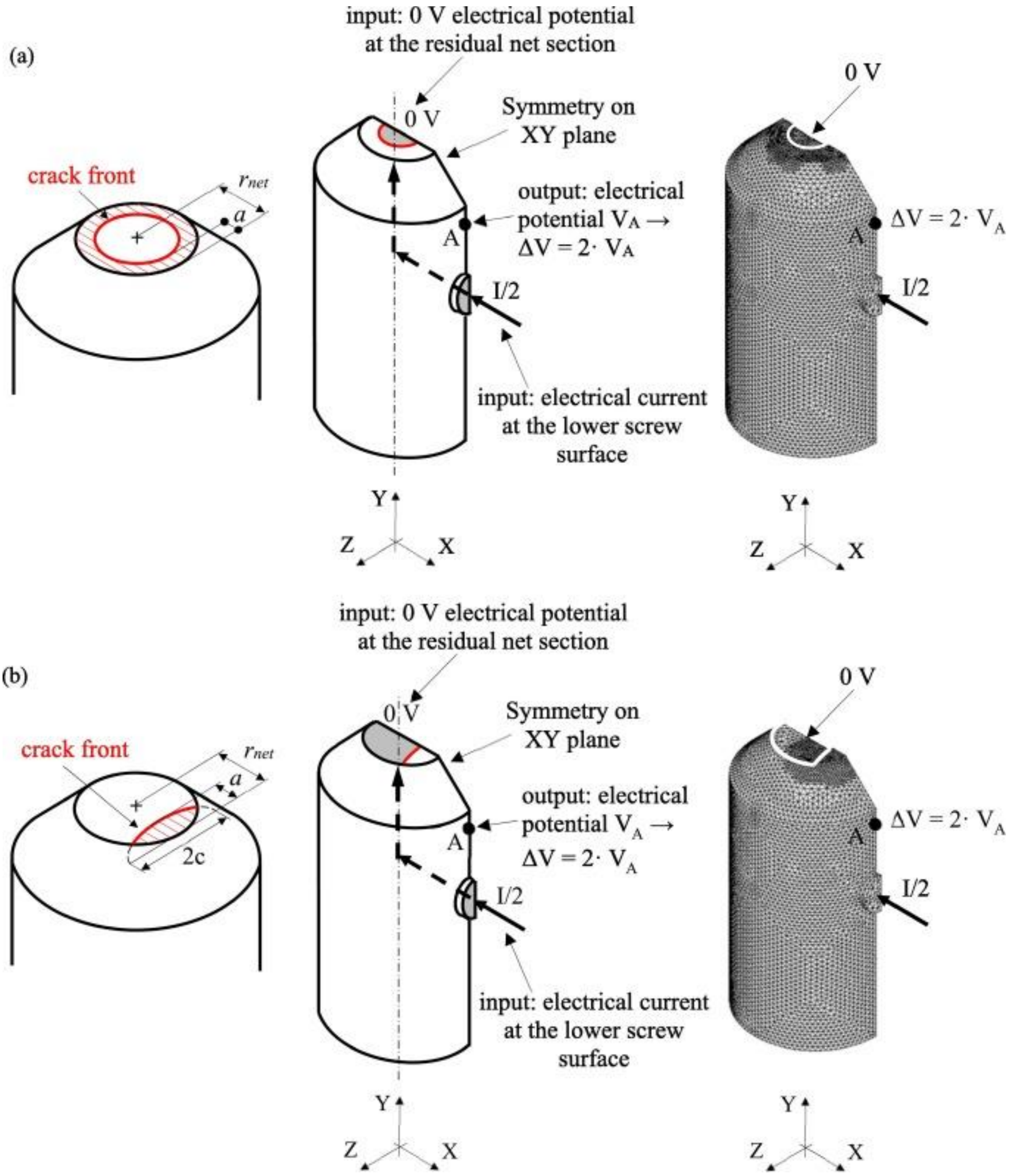
(a)
input: 0 V electrical potential at the residual net section
0 V
Symmetry on XY plane
crack front
r_{net}
a
output: electrical potential V_A → $\Delta V = 2 \cdot V_A$
A
I/2
input: electrical current at the lower screw surface
0 V
$\Delta V = 2 \cdot V_A$
A
I/2
Y
Z
X
Y
Z
X
(b)
input: 0 V electrical potential at the residual net section
0 V
Symmetry on XY plane
crack front
r_{net}
a
2c
output: electrical potential V_A → $\Delta V = 2 \cdot V_A$
A
I/2
input: electrical current at the lower screw surface
0 V
$\Delta V = 2 \cdot V_A$
A
I/2
Y
Z
X
Y
Z
X

Fig. 12. Electrical FE analyses to derive the calibration curves of the potential drop method in the case of (a) a circumferential and (b) a semi-elliptical crack. Considered case: sharp V-notched specimen ($\rho = 0.1$ mm).

To evaluate the potential drop relevant to the uncracked configuration ΔV_0, first the electrical FE analyses with $a = 0$ have been carried out and the potential drop V_A of Fig. 12 has been calculated. Obviously, the potential drop ΔV_0 has to be evaluated as $2\,V_A$, due to the anti-symmetry boundary conditions applied.

Afterwards, several electrical FE analyses have been performed by modelling a crack depth *a* at the net-section as illustrated in Fig. 12, which was varied between 0.1 and 5 mm. In agreement with the observations of the fracture surfaces reported in previous Fig. 6, two different crack shapes have been modelled: (i) a circumferential crack (see Fig. 12a) valid for torsion and combined bending-torsion fatigue loadings; and (ii) a semi-elliptical crack (see Fig. 12b) valid for axial and bending fatigue loadings. To properly set the aspect ratio *c*/*a* of the elliptical crack shape of the latter case, one fatigue test under pure bending with $\Delta\sigma = 490$ MPa and another one under pure axial loading with $\Delta\sigma = 270$ MPa, have been stopped at $N_i = 29800$ cycles and 160200 cycles, respectively, corresponding to a $\Delta V/\Delta V_0$about equal to 1.01. Then, both specimens have been brought to failure under static conditions, to analyse the initiated crack by means of a digital microscope. The results are shown in Fig. 13a and b, where it can be observed that the aspect ratio *c*/*a* is equal to approximately 10 under pure bending loading, while it is approximately 3 under pure axial loading. Accordingly, the aspect ratios $c/a = 3$ and 10 have been adopted in the electrical FE analyses.

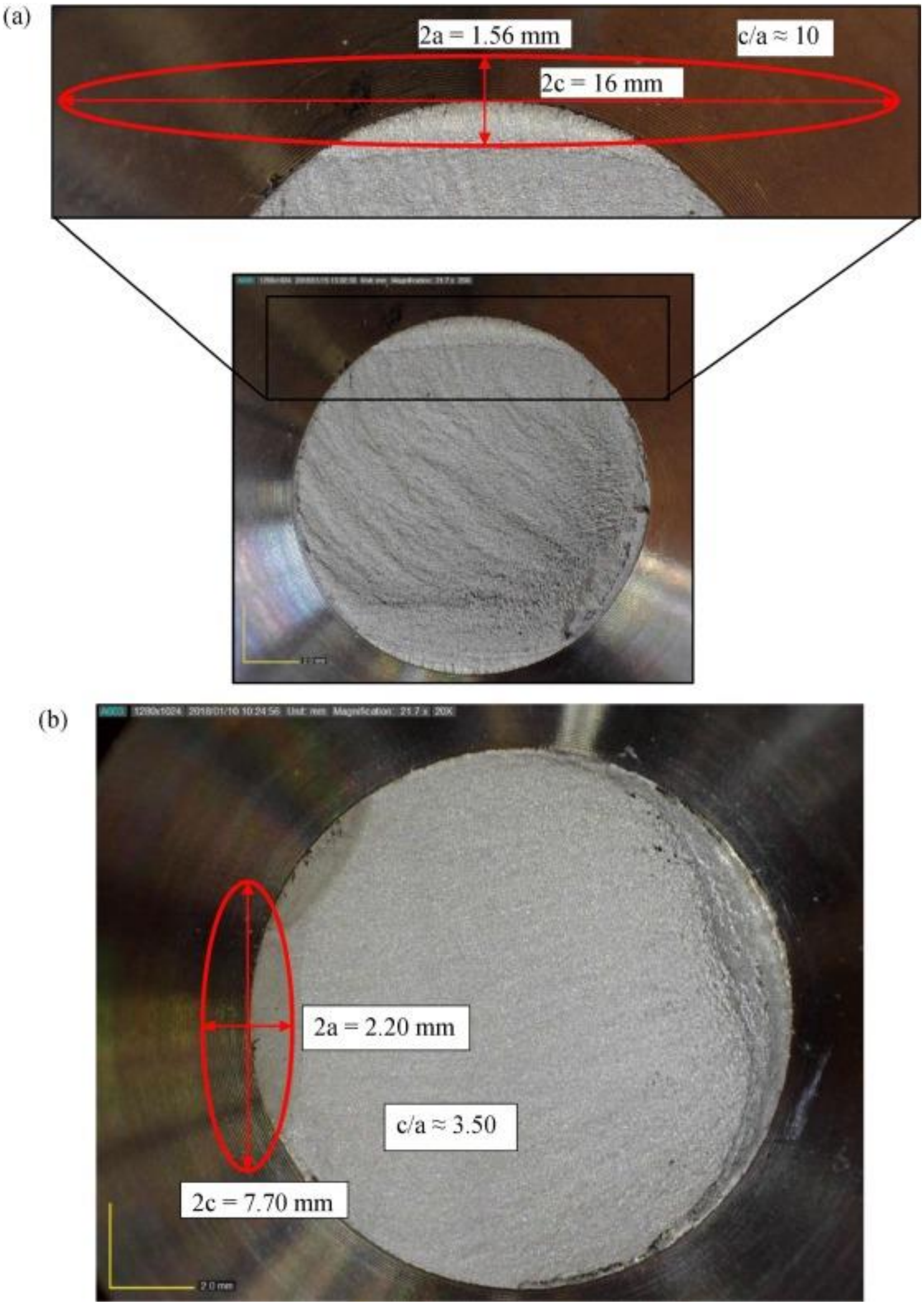
(a)
2a = 1.56 mm
c/a ≈ 10
2c = 16 mm
(b)
A003 1280x1024 2018/01/10 10:24:56 Unit: mm Magnification: 21.7 x 20X
2a = 2.20 mm
c/a ≈ 3.50
2c = 7.70 mm
2.0 mm

Fig. 13. Experimental measurement of the aspect ratio *c*/*a* of semi-elliptical cracks obtained by fatigue testing two sharp V-notched specimens under (a) bending loading with $\Delta\sigma = 490$ MPa and (b) axial loading with $\Delta\sigma = 270$ MPa. Tests have been stopped when $\Delta V/\Delta V_0 = 1.01$, then specimens have been fractured under static conditions.

By applying the same boundary conditions adopted previously to analyse the un-cracked specimen geometries, the potential drop V_A of Fig. 12 has been calculated from the FE analyses. Finally, the potential drop ΔV has been evaluated as $2\,V_A$.

A summary of all electrical FE analyses performed is reported in Table 4. Fig. 14a and b report the obtained results in terms of ratio $\Delta V/\Delta V_0$ as a function of the normalized crack depth a/r_{net}, r_{net} being the radius of the net-section. An experimental validation of the obtained calibration curves has been recently carried out in [65], where a quite good agreement between numerical and experimental measurements has been obtained.

Table 4. Summary of the electrical FE analyses to calibrate the potential drop method; results are reported in Fig. 14, Fig. 15.

Specimen code	**a (mm)**	**r_{net} (mm)**	**Crack shape**	**c/a (–)**	**Valid for load type***
SN_ρ0.1_d_{net}^{12}	0, 0.1–5	6	Circumferential	–	T, B + T
			Semi-elliptical	10	B
BN_ρ4_d_{net}^{12}	0, 0.1–5	6	Circumferential	–	T, B + T
			Semi-elliptical	10	B
SN_ρ0.1_d_{net}^{13}	0, 0.1–5	6.5	Circumferential	–	T
			Semi-elliptical	3	A

*

A = axial, B = bending, T = torsion, B + T = combined bending-torsion.

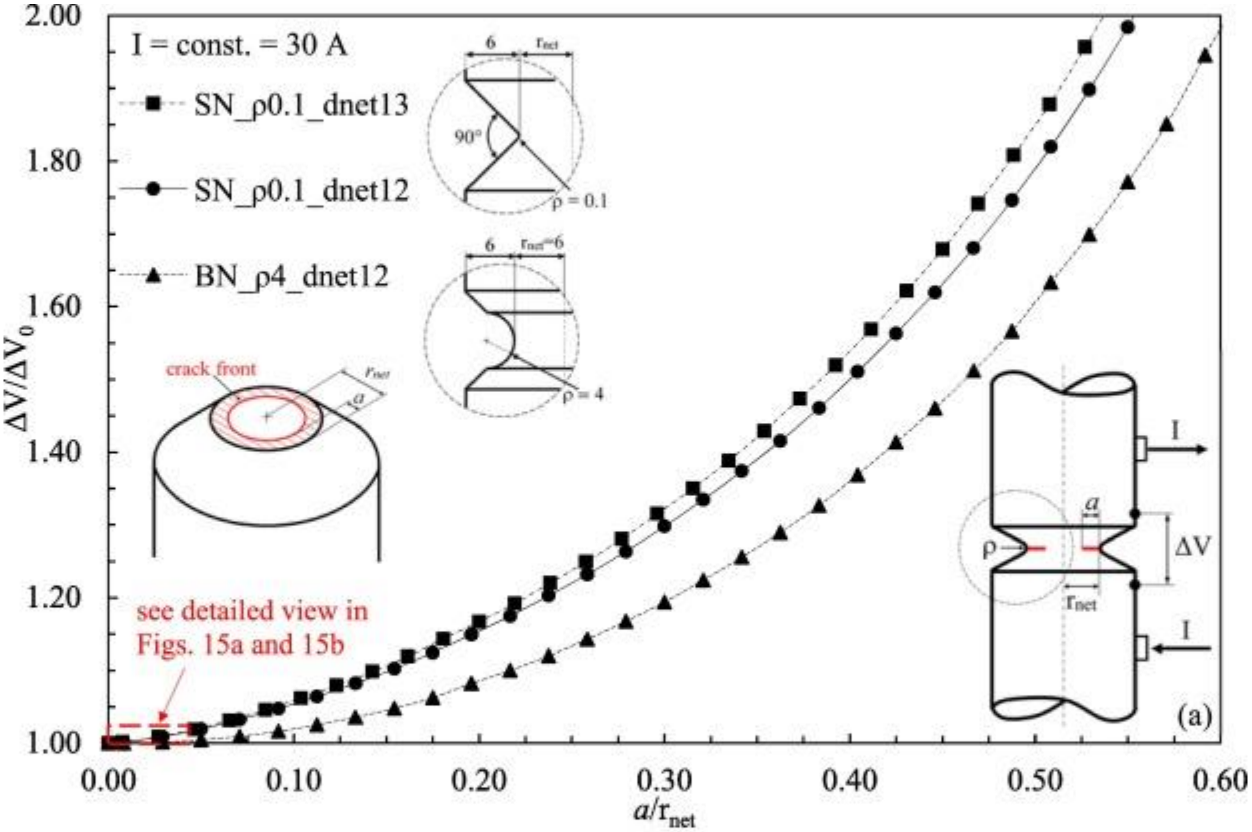
I = const. = 30 A
SN_ρ0.1_dnet13
SN_ρ0.1_dnet12
BN_ρ4_dnet12
6
r_net
90°
ρ = 0.1
6
r_net=6
ρ = 4
crack front
r_net
a
see detailed view in
Figs. 15a and 15b
I
a
ρ
ΔV
r_net
I
(a)
ΔV/ΔV_0
1.00
1.20
1.40
1.60
1.80
2.00
0.00
0.10
0.20
0.30
0.40
0.50
0.60
a/r_net

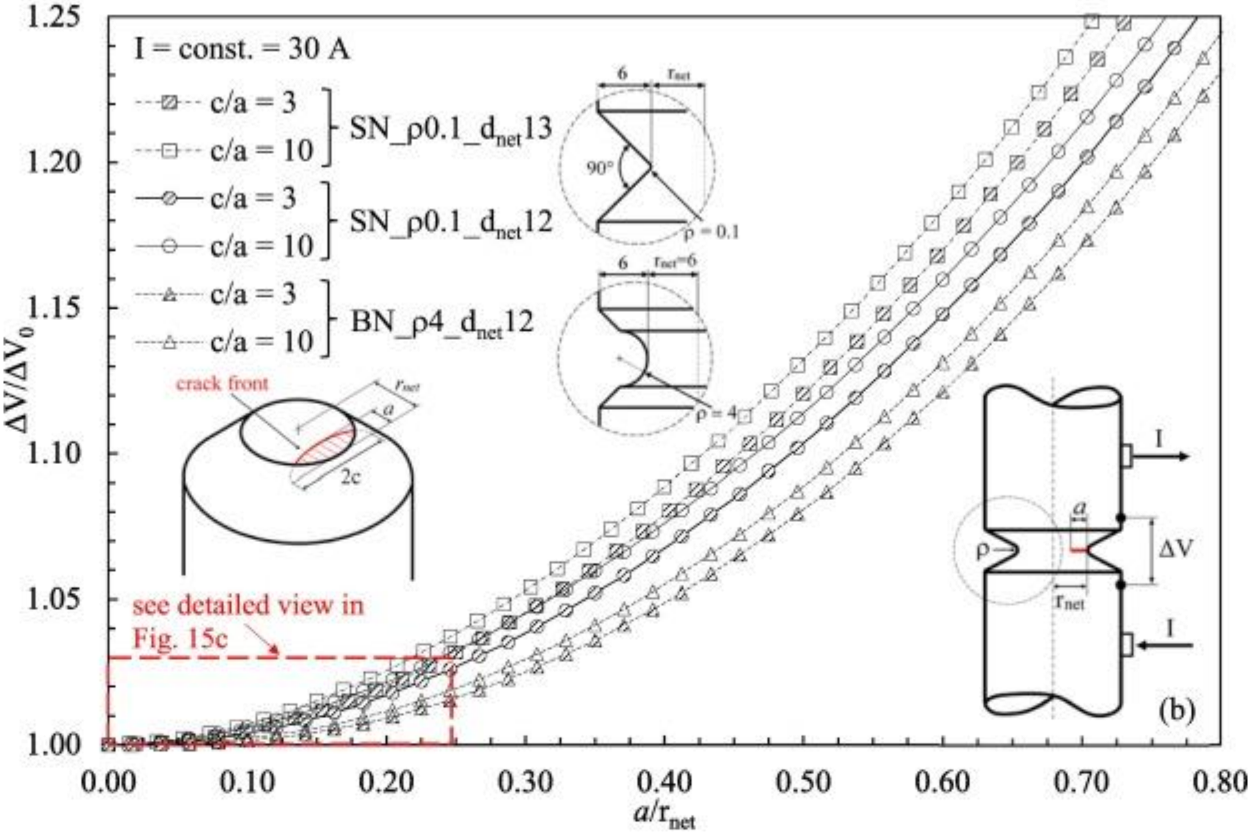
I = const. = 30 A
c/a = 3
c/a = 10
SN_ρ0.1_d_net13
c/a = 3
c/a = 10
SN_ρ0.1_d_net12
c/a = 3
c/a = 10
BN_ρ4_d_net12
6
r_net
90°
ρ = 0.1
6
r_net=6
ρ = 4
crack front
r_net
a
2c
see detailed view in
Fig. 15c
I
a
ρ
ΔV
r_net
I
(b)
ΔV/ΔV_0
1.00
1.05
1.10
1.15
1.20
1.25
0.00
0.10
0.20
0.30
0.40
0.50
0.60
0.70
0.80
a/r_net

Fig. 14. Calibration curves of the potential drop method obtained numerically in terms of $\Delta V/\Delta V_0$ as a function of the normalized crack depth a/r_{net} for (a) a circumferential crack and (b) a semi-elliptical crack. ΔV_0 represents the electrical potential of the reference un-cracked specimen ($a = 0$).

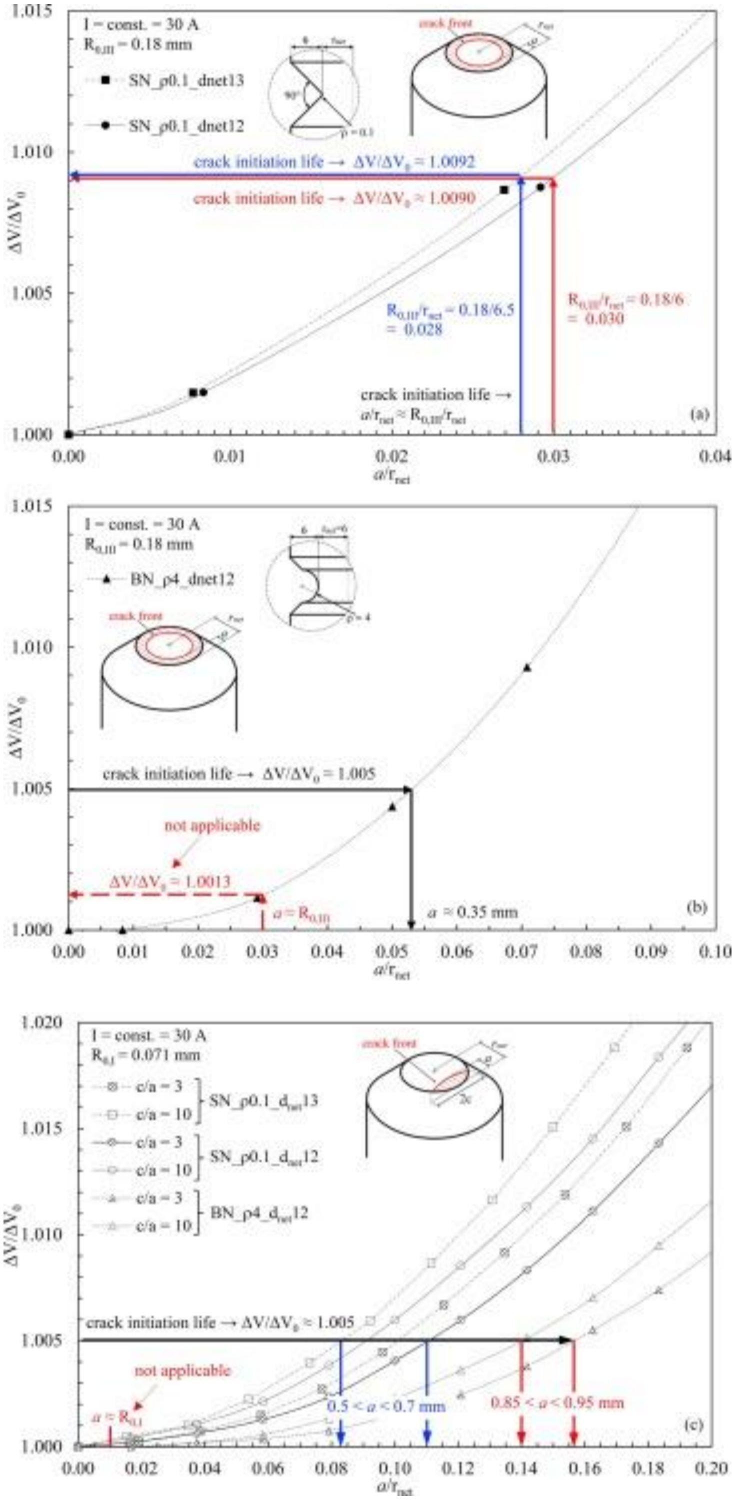

1. Download high-res image (461KB)
2. Download full-size image

Fig. 15. Detailed views of previous Fig. 14. Definition of physical crack initiation life for (a) a circumferential crack in sharp notched specimens, when $a \approx R_{0,III}$; definition of technical crack initiation life for (b) a circumferential crack in blunt notched specimens

and (c) a semi-elliptical crack in both sharp and blunt notched specimens, when $\Delta V/\Delta V_0 \approx 1.005$.

The calibration curves reported in Fig. 14a and b coupled with the experimentally measured ratio $\Delta V/\Delta V_0$ as a function of the number of loading cycles (see examples in Fig. 9), allow a physical definition of the crack initiation life consistent with the SED approach, i.e. when the initiated crack depth a equals the structural volume size R_0. The control radii being different under mode I and mode III loadings, initiation life has been defined according to the following rules:

- $a \approx R_{0,I} = 0.071$ mm in the case of pure bending or pure axial fatigue loadings;
- $a \approx R_{0,III} = 0.18$ mm in the case of pure torsion fatigue loadings;
- $a \approx \max\{R_{0,I}, R_{0,III}\}$ in the case of combined bending-torsion fatigue loadings, i.e. $a \approx R_{0,III} = 0.18$ mm in the present case.

Dealing with sharp V-notches under pure torsion and combined bending-torsion loadings, Fig. 15a shows that the physical definition of the crack initiation life ($a \approx R_{0,III} = 0.18$ mm) corresponds to a relative potential drop increase $\Delta V/\Delta V_0$ approximately equal to 1%. On the other hand, in the case of blunt notches under pure torsion and combined bending-torsion loadings Fig. 15b shows that the definition of the crack initiation life when $a \approx R_{0,III}$ would correspond to a ratio $\Delta V/\Delta V_0$ about equal to 0.13%. Unfortunately, such a reduced value is not applicable due to the un-sufficient sensitivity of the adopted DCPD crack growth monitor device. Therefore, in the case of blunt notches under pure torsion and combined bending-torsion loadings a technical definition has been adopted for the crack initiation life, i.e. at a potential drop increase equal to 0.5%, this ratio corresponding to a crack depth a about equal to 0.35 mm (see Fig. 15b).

Regarding pure bending and pure axial loadings, it should be noted that the potential drop method is less sensitive to the initiation of an elliptical crack than to the initiation of a circumferential one (calibration curves of Fig. 14b should be compared with those of Fig. 14a) and that the control radius $R_{0,I}$ is much lower than $R_{0,III}$. That said, Fig. 15c shows that the physical definition of the crack initiation life ($a \approx R_{0,I} = 0.071$ mm) would correspond to a relative potential drop increase $\Delta V/\Delta V_0$ lower than 0.05%. Again, such a reduced value is not applicable. Therefore, also in the case of pure bending and pure axial loadings the technical definition of the crack initiation life, i.e. $\Delta V/\Delta V_0 = 0.5\%$, has been adopted. According to Fig. 15c, this ratio corresponds to a crack depth *a* in the range 0.5–0.7 mm in the case of sharp V-notches and in the range 0.85–0.95 mm for blunt notches.

The crack initiation life, N_i, defined according to Fig. 15 has been reported in previous Fig. 9, and it has been adopted in Fig. 10b to present the experimental results. Crack initiation life will be adopted in the next section to re-analyse the experimental results by means of the averaged SED approach.

5.3. SED-based analysis of crack initiation life and comparison with total life experimental data

Dealing with plain specimens under pure axial and pure torsion fatigue loadings, the averaged SED values, $\Delta \overline{W}$, have been calculated by substituting the relevant nominal net-section stress range into Eqs. (2), (3), respectively, with $c_w = 0.5$ (the nominal load ratio R being equal to −1).

In the case of notched specimens, the averaged SED values have been calculated using the direct approach, $\Delta \overline{W}$, according to Eq. (9), by applying again $c_w = 0.5$. 2D structural FE analyses have been carried out by means of Ansys® software, by using a 2D, harmonic, 8-node quadrilateral, structural solid element (PLANE 83 of Ansys® element library), as reported in Fig. 16a and b. Coarse FE meshes with about 30 finite elements inside the control volume (see examples in Fig. 16a and b) have been generated by using a FE size $d \approx R_0/2$. Fig. 16a and b report in detail the loads and restraints applied to the FE models to properly simulate the experimental configuration. To calculate the energy contribution due to bending loading and averaged over a structural volume with size $R_{0,I}$ (see Fig. 16c), 3D structural FE analyses were needed due to the application of non axis-symmetric loadings. Fig. 16c reports an example of the adopted FE mesh, along with a detail of the structural volume for averaged SED calculation. Only a quarter of the specimen has been modelled, anti-symmetry on YZ plane and symmetry on XY plane (see Fig. 16c) being applied. The loads and restraints applied by the adopted flexible test bench (see Fig. 4) have been simulated by fixing the cylindrical surface highlighted in gray in Fig. 16c and by applying the range value of the experimental bending moment, ΔM_b, through concentrated forces at the opposite end. It should be noted that the examples reported in Fig. 16 are relevant to sharp notches; in the case of blunt notches, the same analysis procedure has been adopted, however a structural volume having the crescent shape defined in previous Fig. 1c has been modelled at the notch tip to calculate the averaged SED.

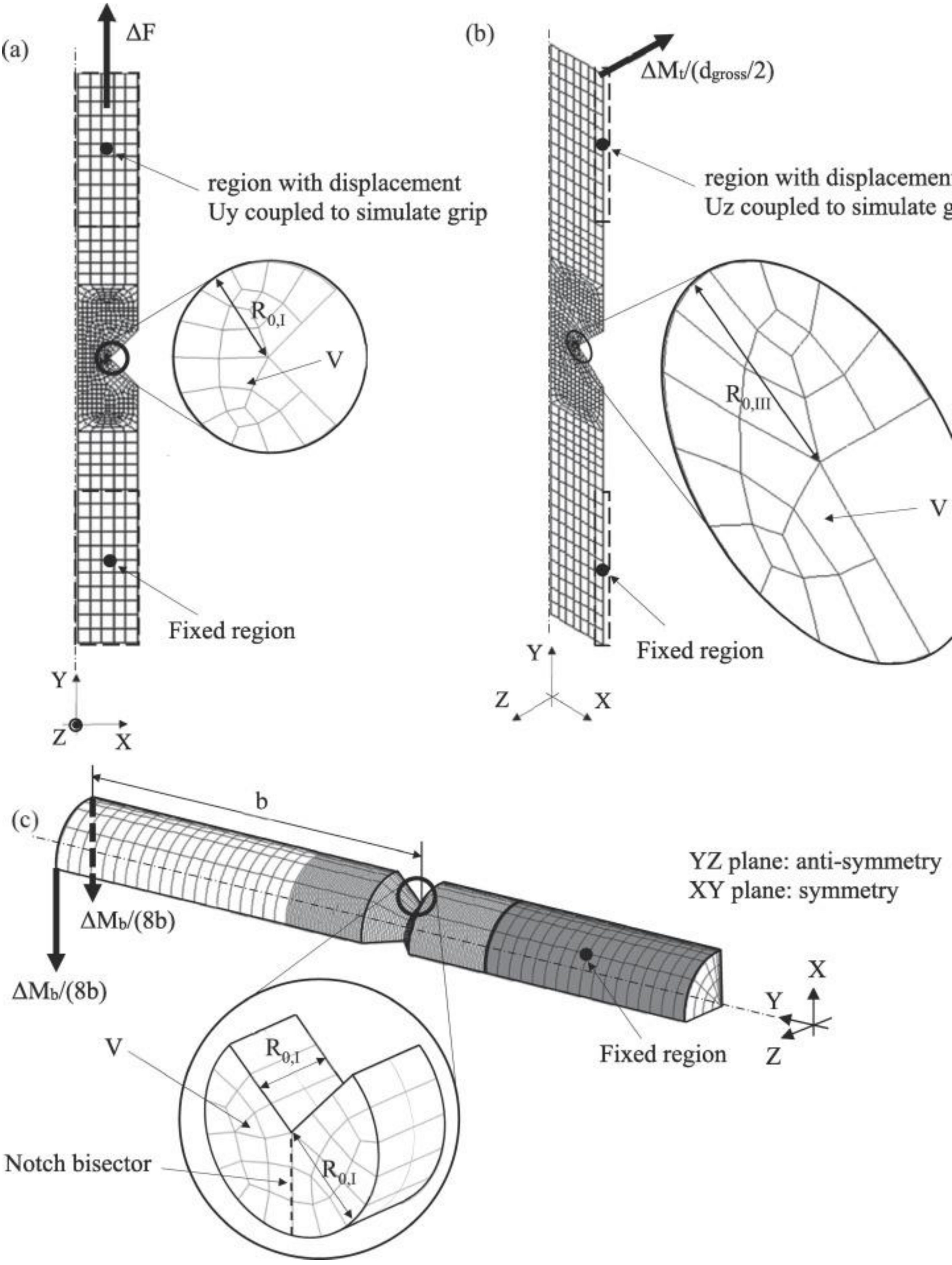
(a)
ΔF
region with displacement
Uy coupled to simulate grip
$R_{0,I}$
V
Fixed region
Y
Z
X
(b)
$\Delta M_t/(d_{gross}/2)$
region with displacemen
Uz coupled to simulate g
$R_{0,III}$
V
Fixed region
Y
Z
X
(c)
b
$\Delta M_b/(8b)$
$\Delta M_b/(8b)$
YZ plane: anti-symmetry
XY plane: symmetry
Fixed region
X
Y
Z
V
$R_{0,I}$
Notch bisector
$R_{0,I}$

1. Download high-res image (961KB)
2. Download full-size image

Fig. 16. Structural FE analyses to evaluate the averaged SED. Coarse FE meshes (about 30 FE inside the control volume) have been adopted in the 2D FE models under (a) axial and (b) torsion loadings and in the 3D FE model under (c) bending loading. The applied loads and restraints simulate the experimental test configuration. Considered case: sharp V-notched specimen ($\rho = 0.1$ mm), $R_{0,I} = 0.071$ mm and $R_{0,III} = 0.18$ mm.

All available experimental fatigue results were converted in terms of averaged SED and have been reported in Fig. 17a, in terms of total fatigue life, and in Fig. 17b in terms of crack initiation life, defined according to Fig. 15.

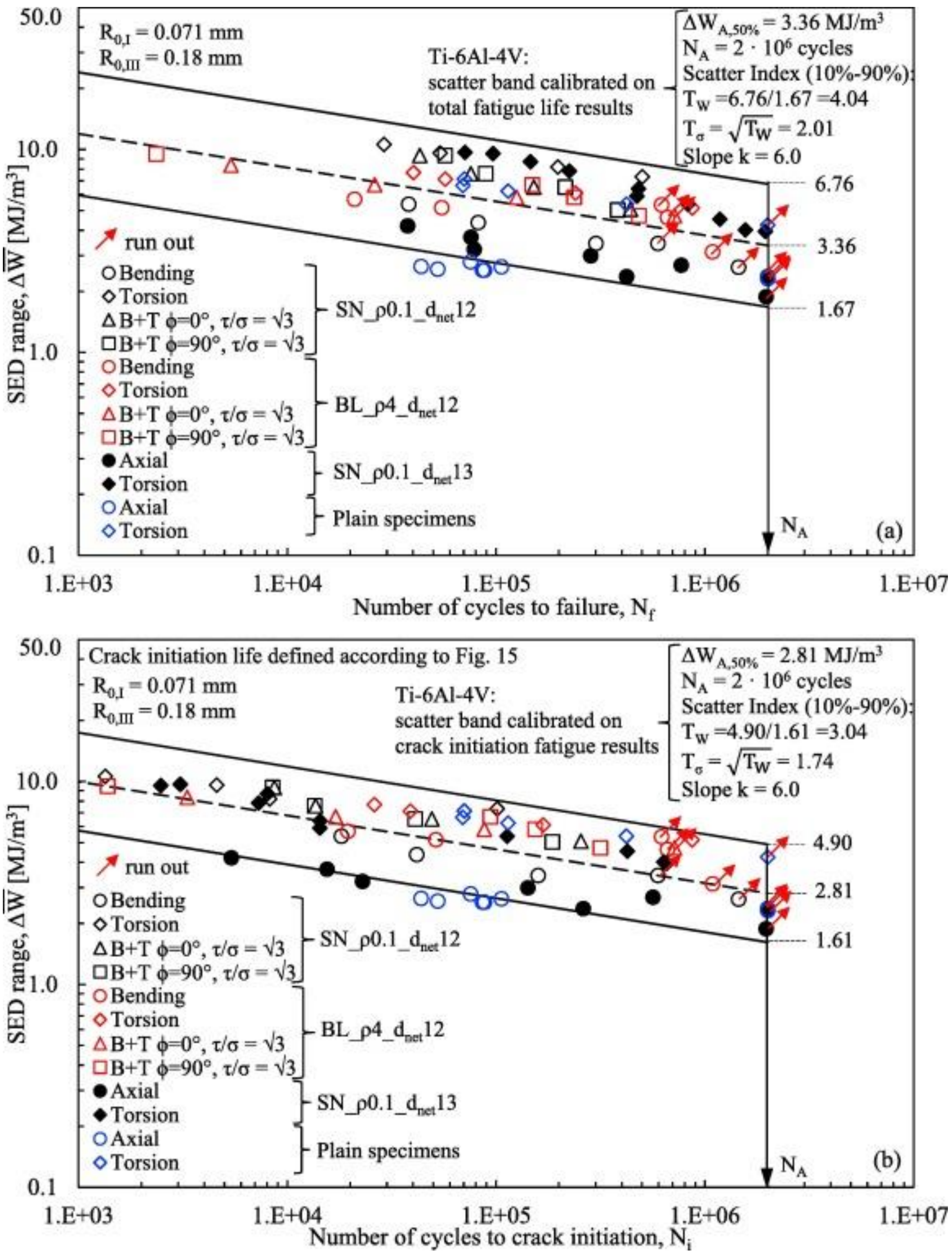

1. Download high-res image (970KB)
2. Download full-size image

Fig. 17. Averaged SED-based scatter-bands calibrated on the experimental results expressed in terms of (a) total fatigue life and (b) crack initiation life, the latter being defined according to Fig. 15.

The averaged SED-based scatter-band fitted on total life data is characterized by a scatter index $T_W = 4.04$, i.e. an equivalent stress-based scatter index $T_\sigma = Tw = 2.01$. By using the crack initiation data, Fig. 17b highlights that the scatter index is reduced, T_W being equal to 3.04 which corresponds to $T_\sigma = Tw = 1.74$, which is slightly higher than 1.40, i.e. the intrinsic fatigue scatter of the crack initiation data evaluated by normalising all available experimental data.

The comparison between Fig. 17a and b suggests that the approach based on the averaged SED coupled with a physical definition of crack initiation life, at least when applicable, is useful to summarise the different notch effects under both uniaxial and multiaxial loading conditions.

6. Conclusions

The local fatigue criterion based on the strain energy density (SED) averaged over a structural volume has been adopted to re-analyse some new experimental multiaxial fatigue results obtained from circumferentially notched specimens made of titanium grade 5 alloy, Ti-6Al-4V. Notched bars with different notch tip radii, namely 0.1 and 4 mm, have been fatigue tested under pure bending, pure torsion and in-phase as well as out-of-phase combined bending-torsion loadings. Crack initiation and propagation have been monitored by using the direct current electrical potential drop (DCPD) method. The following conclusions can be drawn:

- According to the DCPD results, the fatigue life spent to initiate the crack under pure bending resulted almost equal to 50% and 90% of the total fatigue life for sharp and blunt notches, respectively. Conversely, under torsion and combined bending-torsion loadings, the initiation life covered only a small portion (about 10–20%) of the total life for sharp notches, while it resulted almost equal to 60–70% of the total fatigue life for blunt notches.
- The phase-shift angle between bending and torsion stresses has almost no influence on the fatigue strength of the considered titanium alloy specimens; it has been found that experimental fatigue results obtained under in-phase ($\phi = 0$) and out-of-phase ($\phi = 90°$) multiaxial loadings fall in the same scatter.

- The size of the structural volume for averaged SED calculation has been determined by fatigue testing plain as well as sharp notched specimens under pure axial and pure torsion loadings. Two different values, namely $R_{0,I} = 0.071$ mm and $R_{0,III} = 0.18$ mm, have been obtained under mode I and mode III loadings, respectively.

- The calibration curves reporting the potential drop vs the crack size were determined by means of electrical FE analyses. Driven by the experimental analysis of fracture surfaces, a circumferential crack shape was assumed under pure torsion and combined bending-torsion loading, while a semi-elliptical crack shape was assumed under pure bending and pure axial loading, the eccentricity being higher in the former case. These engineering assumptions represent an idealization of the actual more complicated material cracking behavior.

- In principle, after calibrating the potential drop method, the physical definition of crack initiation life (i.e. when the initiated crack depth *a* equals the structural volume size) could have been applied. In practice, the following procedure was adopted: for sharp V-notches under pure torsion and combined bending and torsion loading, initiation life was defined uniformly, i.e. when the crack size equaled $R_{0,III}$. On the other hand, for blunt notches under all loading conditions and for sharp V-notches under pure bending and pure axial loading, the physical definition of crack initiation could not be applied, the required potential drop increase resulting too small to measure with the adopted DCPD equipment. Therefore, a technical crack initiation life has been adopted, consisting in a potential drop increase of 0.5%.

- Finally, the crack initiation life has been considered in the averaged SED-based re-analysis with the aim of reducing the effects of extrinsic mechanisms acting during the crack propagation phase, i.e. sliding contact, friction and meshing between crack surfaces, which were highlighted during experimental tests by powder and debris emanated from the notch tip under torsion and out-of-phase multiaxial fatigue tests. By adopting the crack initiation life, a significant reduction of scattering has been obtained in the SED-based re-analysis, the scatter index T_σ being 14% lower than that obtained in the synthesis of total fatigue life data.